Robust and Superelastic Spider Web-Like Polyimide Fiber Based Conductive Composite Aerogel for Extreme Temperature Tolerant Linear Pressure Sensor

Journal:	*SCIENCE CHINA Materials*
Manuscript ID	SCMs-2022-1912.R1
Manuscript Type:	Article
Date Submitted by the Author:	11-Jan-2023
Complete List of Authors:	Liu, Hu; Zhengzhou University Yang, Wenke; Zhengzhou University Du, Houyi; Zhengzhou University Zhang, Minyue; Zhengzhou University Wang, Chunfeng Yin, Rui; Zhengzhou University PAN, Caofeng; Chinese Academy of Sciences, Beijing Institute of Nanoenergy and Nanosystems Liu, Chuntai; Zhengzhou University Shen, Changyu; Zhengzhou University
Keywords:	Polyimide fiber, Superelastic aerogel, Pressure sensor, Linear sensing, Environmental tolerance
Speciality:	functional polymer composites

Note: The following files were submitted by the author for peer review, but cannot be converted to PDF. You must view these files (e.g. movies) online.

Video S1.mp4
Video S2.mp4
Video S3.mp4
Video S4.mp4
Video S5.mp4

Robust and Superelastic Spider Web-Like Polyimide Fiber Based Conductive Composite Aerogel for Extreme Temperature Tolerant Linear Pressure Sensor

Wenke Yang,[1,2] Hu Liu,[1,2*] Houyi Du,[1] Minyue Zhang,[1] Chunfeng Wang,[3] Rui Yin,[1,4]

Caofeng Pan,[2*] Chuntai Liu,[1*] Changyu Shen[1]

[1]Key Laboratory of Materials Processing and Mold (Zhengzhou University), Ministry of Education; National Engineering Research Center for Advanced Polymer Processing Technology, Zhengzhou University, Zhengzhou, Henan 450002, China

[2]CAS Center for Excellence in Nanoscience, Beijing Key Laboratory of Micro-nano Energy and Sensor, eenennstitute of Nanoenergy and Nanosystems, Chinese Academy of Sciences, Beijing 101400, China

[3]College of Physics and Optoelectronic Engineering, Shenzhen University, Shenzhen 518060, China

[4]China Astronaut Research and Training Center, Beijing 100094, China

*: *Correspondence authors*

E-mail addresses: liuhu@zzu.edu.cn (H. L.); cfpan@binn.cas.cn (C. P.); ctliu@zzu.edu.cn (C. L.)

Abstract

Pressure sensor represents cornerstone of artificial tactile sensing. Extensive researches have been made toward high-performance pressure sensor, however, the settlement of high sensitivity, wide linear response range, and wide working temperature range still remains a huge challenge. Here, triethylamine was innovatively applied to achieve the homogeneous dispersion of hydrophobic polyimide fiber (PIF) in CNTs aqueous dispersion without deteriorating the structure of fiber, and a robust and superelastic spider web-like PIF/CNTs conductive composite aerogel is developed using the freeze-drying and thermal imidization technique for pressure sensor with the merits of wide linear sensing range (0.01-53.34 kPa), ultralow detection limit (10 Pa), high sensitivity (0.507 kPa^{-1}), fast response/recovery time (85/80 ms), stable fast compression response (500 mm/min), and excellent cyclic fatigue resistance (5000 times). Finite-element analysis indicates that the hierarchical fibrous network facilities a significant linear variation in the contact area between adjacent conductive fiber upon external pressure, as well as contributes to the excellent linear sensing capacity. The pressure sensor is demonstrated to be applicable in human physiology and motion signal detection, electronic skin, and intelligence control. Notably, it also exhibits amazing sensing stability and thermal insulation under extreme temperature, demonstrating much promise for emerging applications such as the sensing unit of space suit and inflatable structures of lunar/mars habitat. This work provides a simple but powerful strategy for developing next the generation linear pressure sensor.

Keywords: Polyimide fiber; Superelastic aerogel; Pressure sensor; Linear sensing;

Environmental tolerance

1 Introduction

Advances in internet of things are enabling an enormous development of artificial tactile sensing technology [1], and the pressure sensor as the cornerstone has attracted widespread attention due to their emerging applications in the fields of remote human health monitoring, human-computer interface, wearable electronic devices, and humanoid robotics [2,3]. Recently, multiple mechanisms including piezoresistive [4], piezoelectric [5], triboelectric [6], and capacitive [7] have been proposed for the pressure sensor, among which the piezoresistive sensor shows great advantages of simple measurement scheme and relatively high reliability, gaining huge attentions. However, achieving a low detection limit and wide pressure sensing range simultaneously is always of great challenge for piezoresistive pressure sensor, limiting its practical application in electronic skin that usually needs both the slight tactile sensation of 1-10 Pa and the sensing of drastic behaviors such as grasping heavy objects (hundreds of kPa) [8]. Besides, piezoresistive pressure sensor with good linear sensing mode and high sensitivity is also in urgent needed for easy signal reading and identification.

Conductive polymer composites (CPCs) based piezoresistive pressure sensor, which outputs resistance sensing signal based on the external pressure induced conductive network variation, has aroused great attentions due to their advantages in easy of processing, good flexibility, and signal collection [9]. More importantly, all the aforementioned challenges of piezoresistive pressure sensor can be expected to be solved via tunning the components ratio and structure of

CPCs rationally, and the 3D porous CPCs with the merits of high compressibility, good recoverability, and lightweight turns to be promising candidates for high-performance piezoresistive pressure sensor, which is closely associated with the contact/separation effect between adjacent conductive skeletons upon compression/release [10,11]. However, there are still two important problems needed to be solved before the propelling of CPCs to piezoresistive sensor. One is the low sensitivity under high pressure due to the densification of porous structure that led to faint resistance change, another one is the trade-off between compression strength and elasticity that make it hard to obtain highly compressible/resilient pressure sensor with high compressive strength. Lots of researches on the optimal design of porous structure has been conducted, aiming to acquire enhanced pressure sensing performances [12]. Inspired by the robust and elastic spider web, stiff ceramic and hard carbon based aerogels with porous fibrous network structure have been successfully fabricated, achieving the superelasticity, high strength, and good resilience, simultaneously [13]. Meanwhile, hierarchical porous structure composed of different pore sizes is also an effective strategy to enable more stress transfer along the small pores to achieve significant variation in conductive paths under small pressure. For instance, hierarchical porous nanocellulose nanofiber-based aerogel modified with stiff polymethylsilsesquioxane displays an excellent compressibility (99%), high compression strength (400.5 kPa), and superelasticity [14]. Among polymeric materials, extreme environment (fire, radiation, chemical corrosion, low and high temperature, etc.) tolerant stiff polyimide fiber (PIF) was considered to be an ideal candidate, and PIF/MXene conductive composite aerogel with a "layer-strut" architecture was first reported by our group for high-performance piezoresistive

sensor [15], but the linearity and sensitivity in the whole pressure range are still not well solved.

Herein, we reported a spider-web like conductive composite aerogel with hierarchical fibrous network using the high modulus but flexible polyimide fiber (PIF) and 1D carboxylic carbon nanotubes (CNTs) as building block and conductive filler, respectively. The premise of our design is the homogeneous dispersion of hydrophobic PIF in CNTs aqueous dispersion, which is resolved perfectly with the help of triethylamine (TEA) without deteriorating the PIF. Moreover, strong interfacial adhesion of PIF-PIF and PIF-CNTs was achieved with the assistance of soluble PAA after a thermal imidization process. After a freeze-drying and thermal imidization process, a robust and superelastic spider web-like PIF/CNTs composite aerogel with a porosity of 99% and density of 13.38 mg•cm^{-3} was successfully fabricated, showing outstanding linear sensing mode over a pressure range of 0.01–53.34 kPa, ultralow detection limit (10 Pa), high sensitivity (0.507 kPa^{-1}), fast response/recovery time (85/80 ms) and excellent fatigue resistance over 5000 times cyclic compression. The finite-element analysis verified that the significant linear variation in the contact area between adjacent conductive fiber upon external pressure contributes to the outstanding linear sensing mode of the sensor. We also confirmed the potential utility of the sensor in the fields of human physiology and motion signal detection, electronic skin, and intelligent control. Combining the good thermal insulation property and outstanding pressure sensing stability under extreme temperatures, our prepared PIF/CNTs composite aerogel can be applicable in ongoing and near-future aerospace exploration.

2 Experimental sections

***Synthesis of water-soluble PAA*:** PAA was synthesized via the polycondensation procedure of the previous report [16]. Typically, 2 g of 4,4′-Diaminodiphenyl ether (ODA, AR, 98%, Shanghai Aladdin Biochemical Technology Co., Ltd, China) and 2.94 g of 3,3',4,4'-biphenyltetracarboxylic dianhydride (BPDA, AR, 97%, Shanghai Aladdin Biochemical Technology Co., Ltd, China) were dissolved into 25 mL N-Methyl-2-pyrrolidone (NMP, AR, 97%, Tianjin Kemiou Chemical Reagent Co. Ltd, China) in sequence and reacted in ice-water bath under mechanical stirring for 10 h. Then, 1.4 mL triethylamine (TEA, AR, 99%, Tianjin Damao Chemical Reagent Factory, China) was dropwise added under vigorous stirring for another 2 h to obtain transparent light-yellow viscous PAA solution (13.84 wt.%), which was subsequently dropwise added into 600 mL of deionized water at 0 °C to be precipitated completely. Finally, the resultant precipitate was filtered, washed using DI water and freeze-dried (10 Pa, -80 °C, 72 h) to obtain the white soluble PAA.

***Preparation of PIF*:** Briefly, 200 mg electrospun polyimide fibrous film (Jiangxi Xiancai Nanofibers Technology Co., Ltd, China) was cut into small pieces and soaked into 30 mL dioxane (AR, 99%, Aladdin) overnight, which was then pulverized using a high-speed shear homogenizer (FJ200-SH) at a shear rate of 13000 rpm for 25 min to obtain a yellow suspension. After a freeze-drying (10 Pa, -80 °C, 72 h) process, fluffy PIF with an average diameter of ~ 400 nm (Figure S1) was obtained and stored for further use.

***Preparation of PIF/CNTs composite aerogel*:** Typically, 100 mg of PAA was dissolved in 40 mL of TEA aqueous solution (5 vol.%) under magnetic stirring for 30 min, and then 100 mg of

carboxylic carbon nanotubes (CNTs, −COOH content: 1.23 wt.%, Chengdu Organic Chemicals Co. Ltd, China) was added and ultrasonically dispersed for 20 minutes to obtain a homogeneous PIF/CNTs dispersion. After that, 200 mg of PIF was uniformly mixed with the suspension under magnetically stirring for 20 min, which was then freeze-dried (10 Pa, -80 °C, 48 hours) and thermal imidized through a temperature-programmed process in nitrogen atmosphere (3 °C/min to 150 °C; 1.5 °C/min to 350 °C), obtaining the designed spider web-like PIF/CNTs composite aerogel. Here, a series of pure PIF aerogels with different PAA loadings and PIF/CNTs composite aerogels with different CNTs loadings were also prepared according to the formulations listed in Table S1 and S2. In this work, the prepared pure PIF aerogels and PIF/CNTs composite aerogels were named as PIF-x and PIF/CNTs-y, where x and y represent the weight ratio of PAA/PIF and CNTs/PIF, respectively.

Finite element analysis : FEA was conducted using the commercial ABAQUS/CAE to numerically simulate the contact area variation between adjacent fiber of spider web-like aerogel. The PI fibers were modeled as linear elastic and incompressible neo-Hookean with Young`s modulus $E_{PIF} = 10$ kPa. The Poisson's ratio of PIF model is set to be 0.3. In order to ensure the stability of the values, the friction coefficients of all interface contacts are set to 0 and there is no mutual penetration.

Characterizations **:** Scanning electron microscope (SEM) images were taken by a JEOL JSM-7500F instrument at an accelerating voltage of 5 kV. Fourier transform infrared (FT-IR) spectra were recorded on a Nicolet Nexus 870 instrument in the attenuated total reflection mode. X-ray

photoelectron spectroscopy (XPS) spectra were measured using an X-ray photoelectron spectrometer (Thermo ESCALAB 250XI) with an Al Kα radiation excitation source. X-ray diffraction (XRD) spectra was collected by a X-ray diffraction spectrometer (Ultima IV). Thermal conductivity was measured by a thermal constant analyzer (Hot Disk AB TPS2500S). Thermogravimetric analysis (TGA) was conducted by a thermogravimetric analyzer (NETZSCH STA 449 F5 Jupiter) in air atmosphere with a heating rate of 10 °C min^{-1} from room temperature to 800 °C. Dynamic mechanical analysis (DMA) was performed by a dynamic thermomechanical analyzer (TA Q800) at a heating rate of 5°C min^{-1} in the temperature range of -50 to 300 °C with a set frequency of 1 Hz and a fixed oscillating strain of 2 %. Compression mechanical properties were tested using a universal testing machine (UTM2203) equipped with a 100 N sensor. As shown in Figure S2, pressure sensor is constructed by pasting flexible conductive tape onto both ends of cylindrical PIF/CNTs composite aerogel to serve as electrodes, and conductive silver paste was applied to ensure a good contact between them. In addition, home-made online pressure sensing test system (Figure S3) consisting of universal testing machine (AG-Xplus) equipped with temperature control box (-100-200 °C) and electrochemical workstation (CHI 660) was constructed to evaluate the potential of PIF/CNTs composite aerogel for pressure sensor. Notably, PIF/CNTs-0.5 was used for all the tests unless otherwise specified.

3 Results and Discussions

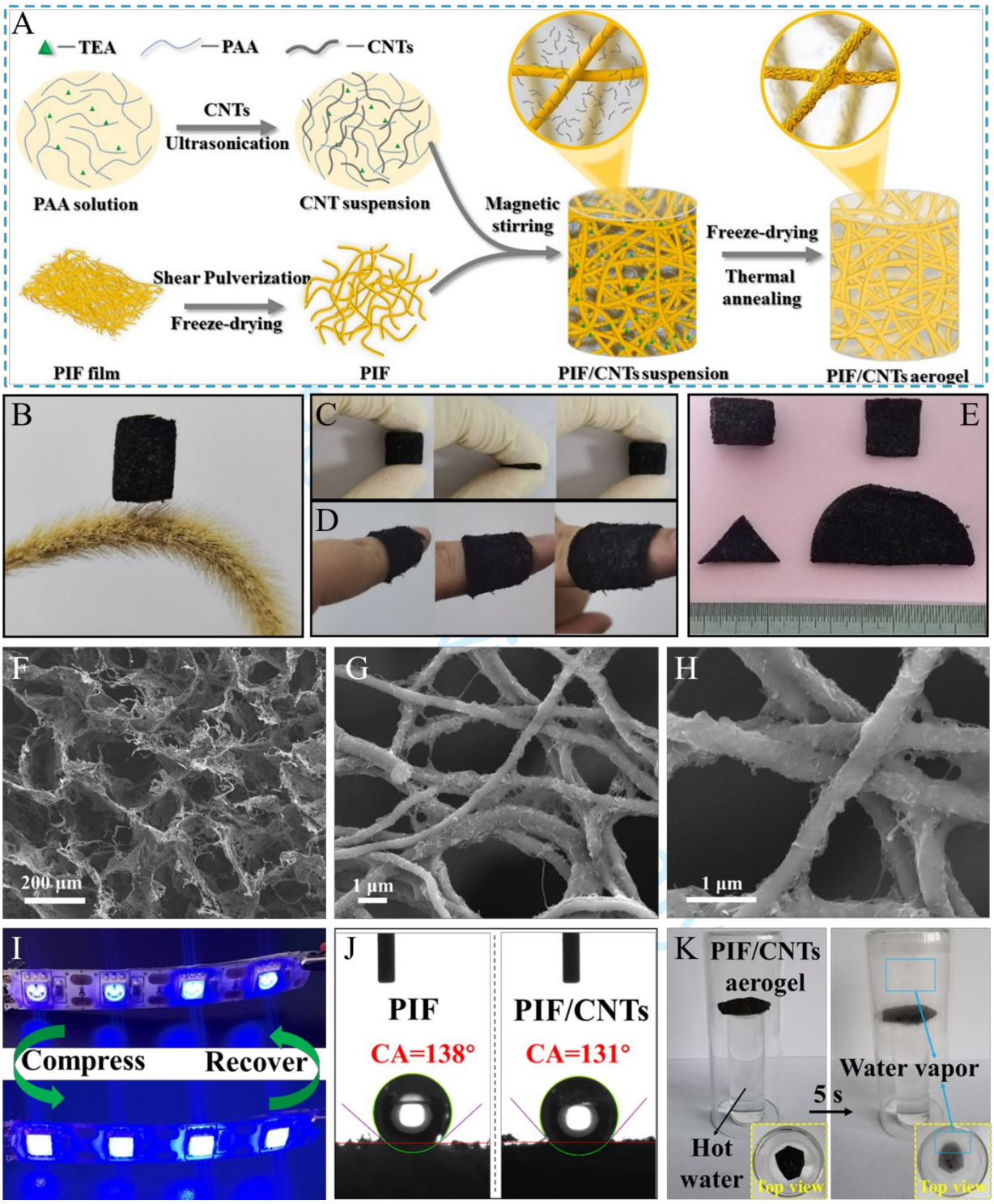

Figure 1. Preparation of PIF/CNTs conductive composite aerogel. (A) Schematic diagram showing the preparation process of the composite aerogel. Digital photos showing the merits of (B) lightweight, (C) compressibility, (D) conformability, and (E) tailorability of the composite aerogel. (F-H) SEM images of the composite aerogel under different magnifications. (I) Brightness change of LED lamp connected with the composite aerogel during cyclic compression process. (J) Water contact angle and Air-permeability test (K) of

the composite aerogel.

Figure 1A depicts the preparation process of PIF/CNTs conductive composite aerogel (see details in the experimental part). In general, the flexible polyimide fiber (PIF) arising from the high-speed shear pulverized polyimide fibrous film was selected as the building block to construct fibrous network, and the water-soluble PAA was introduced to act as glue to ensure the structure stability after the imidization process, with CNTs blending to endow the ideal conductivity. To construct the porous fibrous structure of the conductive composite aerogel, all the components stated above are first homogeneously dispersed into DI water and followed by a freeze-drying process. Here, environment-friendly water is considered to be an ideal dispersant due to its good solubility to PAA and excellent dispersion for carboxylic CNTs (Figure S4), but PIF is inapplicable to water due to its hydrophobicity. The addition of weak alkaline TEA is conductive to improve the wettability of PIF by water, as shown in Figure S5 and S6 and Video S1. TEA aqueous solution can be absorbed quickly after dropping onto the surface of PI fibrous film, where the WCA decreases from 133° for DI water to 0° for TEA aqueous solution, and PIF can be homogenously dispersed into the TEA aqueous solution without obvious aggregation. All these will undoubtly enable the formation of homogeneous and long-term stable PIF/CNTs dispersion and well-structured fibrous conductive composite aerogel.

The thermal imidization is another important step to transfer PAA into PI, which glues the physical connected PIF together strongly. Compared with the PIF aerogel without PAA that is easily to be torn out and compressed into a pellet with poor recoverability, the existence of PAA can significantly enhance its structural stability, robustness, and elasticity (Figure S7).

Meanwhile, the pure PIF aerogel exhibits enhanced compressive mechanical property with increasing the PAA content (Figure S8), showing excellent adjustability to satisfy different application requirements. The cyclic fatigue resistance of PIF aerogel displays a decreasing trend when PAA content goes beyond the threshold value, arising from the excessive high modulus thermal imidized PI which seriously affects the flexibility and elasticity of PIF. Considering the long-term stability of pressure sensor in practical application, an optimal PAA/PIF ratio of 0.5 is fixed in our work. As a result, the black lightweight fibrous PIF/CNTs composite aerogel that can stand on Setaria steadily is successfully fabricated, as displayed in Figure 1B. Meanwhile, its excellent compressibility and recoverability (Figure 1C), good conformability to human body (Figure 1D) and easy tailorability into diverse shapes (Figure 1E) will undoubtly enable it to be applicable for wearable flexible pressure sensor.

It should be noted that our study supplies a simple strategy to achieve the stable dispersion of PIF in water compared with the complicated mixed solvent system and oxygen plasma irradiation, showing great significance to its more widespread applications [17]. To explore the excellent water wettability of PIF with the help of TEA in depth, FT-IR and XPS were conducted and analyzed. As shown in the FT-IR spectra (Figure S9A), obvious hydrophilic $NH(C)_2$ group appears for PIF after being immersed in the TEA aqueous solution (TEA-PIF) [18]. In addition, as shown in the high-resolution XPS spectra of C1s and N1s (Figure S9B&C), the area and intensity of C–N peak becomes stronger, and the hydrophilic $NH(C)_2$ group can also be well observed. However, the hydrophilic $NH(C)_2$ group disappears completely after being thermal

annealed (Figure S10), leaving the characteristic groups of original PIF, indicating that TEA can be completely removed during the thermal imidization process, which can also be confirmed according to the TG curve of PIF aerogel without thermal imidization (Figure S11) [16,19]. Hence, the corresponding wetting mechanism can be illustrated in Figure S12. TEA aqueous solution presents weak alkalinity due to the nucleophilic effect of the lone pair electrons of TEA, causing the open of amide bond of PI and the formation of hydrophilic $NH(C)_2$ group [20]. Here, such an alkalization process is reversible through a simple thermal treatment, enabling the mechanical property of original PIF to be well preserved.

As shown in Figure 1F-H, the designed spider web-like PIF/CNTs conductive composite aerogel with hierarchical fibrous porous structure is successfully constructed, arising from the sublimation of ice crystals that reject the well dispersed PIF and CNTs during the freeze-drying process. Specifically, it exhibits an obvious open cellular structure with a diameter of 200-300 μm (Figure 1F) and spider web-like cell wall with minor pores of 3–5 μm (Figure 1G&H). Here, the typical hierarchical porous fibrous structure is beneficial for the composite aerogel to bear large compression strain, and the spider web-like skeleton gives it sufficient robustness and flexibility. Besides, it can be clearly observed that CNTs are homogeneously distributed on the surface of PIF and thermal imidized PI welds PIF-PIF and PIF-CNTs well, ensuring the construction of stable and robust conductive networks. As a result, cyclic compression of the composite aerogel can lead to the regular brightness change of the connected LED lamp (Figure 1I, Video S2), indicating the large application potential of our prepared fibrous porous structured

PIF/CNTs conductive composite aerogel for high-performance wearable pressure sensor.

Water repellence and moisture permeability are closely related with the wearing comfortability and protection from humid or underwater environments (e.g., sweat, liquid droplet, rain) of wearable electric devices. As shown in Figure 1J, PIF aerogel exhibits a WCA of 138° due to the rough surface and inherent hydrophobicity of PIF, and the WCA of PIF/CNTs composite aerogel exhibits a slight decrease to 131° due to the existence of hydrophilic CNTs, but the hydrophobicity is still well maintained, ensuring the stable electrical property without being disturbed in humid or underwater environments. Besides, it can be impressively seen from Figure 1K that when a glass tube containing hot water is tightly sealed by the composite aerogel, the water vapor can easily pass through the aerogel and condense into water droplets within 5 seconds on the top of glass hood. Such an excellent air permeability is mainly ascribed to the hierarchical porous architecture and excellent hydrophobicity of the prepared composite aerogel for ease of transmitting moisture. According to relevant medical studies, approximately 500 ml of water evaporates from human skin every day. So, the sweat and water vapor can accumulate between the sensor and skin, forming a waterlogged layer that can lead to the drifting of electrical signals and skin discomfort. Therefore, breathability is important for the long-term usability of wearable smart devices. Thermogravimetric analysis (TGA) and derivative thermogravimetric analysis (DTG) curves were analyzed to evaluate their thermal stability of the as-prepared composite aerogel (Figure S13). Clearly, the onset decomposition temperature (T_{onset}=490 °C) and the maximum decomposition rate temperature (T_{max}=571 °C) of the PIF/CNTs composite

aerogel is lower than that of the pure PIF aerogel (T_{onset} =504 °C, T_{max} =581 °C), which can be ascribed to the existence of large amount of CNTs that act as a heat source to accelerate the decomposition of PIF [21]. But it can still endow the PIF/CNTs composite aerogel-based pressure sensor with competitive advantage of high temperature tolerance over other traditional polymer-based aerogels.

To figure out the phase composition and interfacial interaction of the composite aerogel, FT-IR, XRD, Raman, and XPS were systematically conducted and analyzed. Figure S14 shows the XRD diffraction patterns of PIF aerogel and PIF/CNTs composite aerogel. The PIF film displays the sharp characteristic peaks located at 38.3°and 44.5°, confirming the different crystal orientations of the polyimide matrix [22]. After being mixed with CNTs, the typical peaks of CNTs appears at the XRD pattern of PIF/CNTs composite aerogel, verifying the successful preparation of the PIF/CNTs composite aerogel [23]. Raman spectra of PIF aerogel and PIF/CNTs composite aerogel are shown in Figure S15. For the PIF aerogel spectrum, the characteristic peaks at 1386 cm^{-1} and 1616 cm^{-1} represents the C–N stretching vibration of imide ring and aromatic imide ring vibration of the dianhydride moiety, respectively. But the PIF/CNTs composite aerogel only displays two broad peaks located at 1360 cm^{-1} and 1580 cm^{-1} without obvious characteristic peaks of PIF [24]. The phenomenon can be ascribed to the charge transfer between PIF and CNTs that lead to the overlap of their characteristic peaks, indicating the existence of interfacial interaction between them. As for the FT-IR spectra in Figure S16, PIF aerogel displays the characteristic peaks of PI matrix, including C–O stretching vibration at 1237

cm^{-1}, C–N stretching vibration at 1371 cm^{-1}, C=C stretching vibration at 1500 cm^{-1}, and C=O asymmetric vibration at 1716 and 1776 cm^{-1},[11] whereas an obvious blueshift is observed for the C=C and C=O peaks of PIF/CNTs composite aerogel due to the electron withdrawing effect, verifying the existence of hydrogen bonding between PIF and CNTs [25]. The XPS spectra of PIF aerogel and PIF/CNTs composite aerogel in Figure S17A demonstrates the main elements of C, O, and N in PIF, and an increase in C percentage is observed for the composite aerogel due to the addition of CNTs. Figure S17B illustrates the high-resolution XPS spectrum of C1s. Compared with PIF aerogel, significant increase in the C–C/C=C peak intensity and decrease in the intensity ratio of C–N peak to C–O peak are obviously observed for the composite aerogel, indicating the successful introduction of carboxylic CNTs in the composite aerogel [26]. In addition, the C–C/C=C peak and C=O peak of the PIF/CNTs composite aerogel shift to a high binding energy peak, arising from the electron withdrawing effect of hydrogen bonding between carboxylic CNTs and PIF, which is consistent with the FT-IR result.

Generally, filler loading is closely related with the electrical and mechanical properties of the composites. As shown in Figure 2A, the conductivity of PIF/CNTs composite aerogel increases slightly with increasing CNTs loading, which is well coincided with the increased slope of the I-V curves (inset in Figure 2A). In addition, the typical linear characteristic demonstrates the construction of stable conductive network for all composite aerogels, enabling stable signal output when served as pressure sensor. As for the compressive mechanical property shown in Figure 2B and S18, both compressive strength and modulus of PIF/CNTs composite aerogel

exhibit an increasing trend with increasing CNTs loading, which can be ascribed to the instinct high mechanical strength and modulus of CNTs, strong hydrogen bonding between CNTs and PIF, and strong adhesiveness of thermal imidized PI, resulting in effective stress transfer upon external compression.

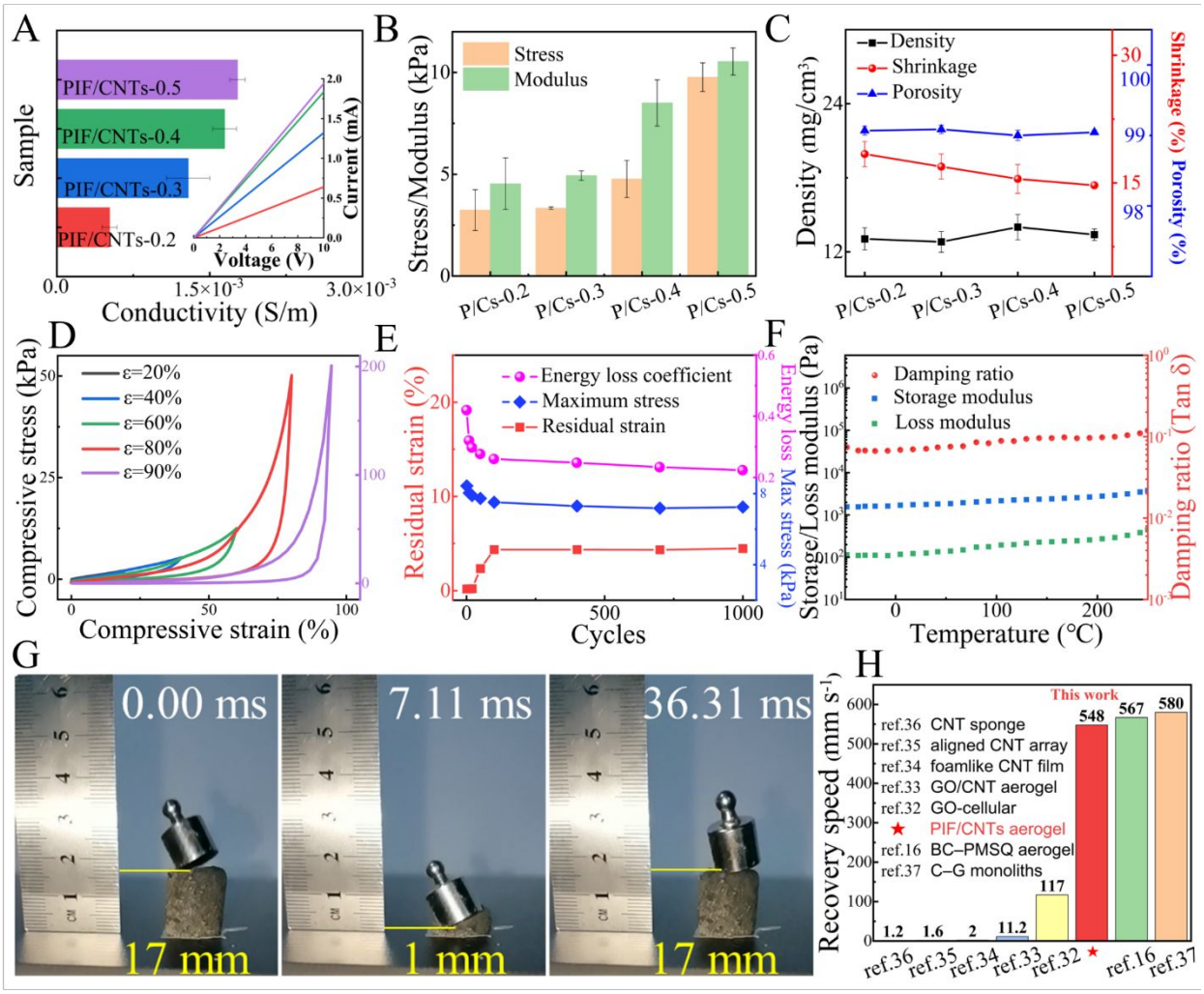

Figure 2. Electrical and mechanical properties of PIF/CNTs composite aerogel. (A) Conductivity and I-V curves, (B) compressive strength and modulus (ε=50%, 20 mm min^{-1}), and (C) density, porosity, and shrinkage rate of PIF/CNTs (P/Cs) composite aerogel with different CNTs loadings. (D) Stress-strain curves of PIF/CNTs-0.5 under stepwise cyclic compression. (E) Residual strain, maximum stress, and energy loss coefficient of PIF/CNTs-0.5 over 1000 cycles. (F) Dynamic compressive viscoelastic properties of PIF/CNT-0.5. (G) Real-time high-speed camera images showing the rebound process of a 10 g weight falls from a height of 10 cm with an initial velocity of 0 m/s. (H) Comparison of the recovery speed of PIF/CNTs composite

aerogel with other published works.

Besides, it can be seen clearly from Figure 2C that the shrinkage rate of composite aerogel exhibits a decreasing trend with increasing the CNTs content, which can be explained by the strengthen effect of CNTs that can effectively inhibits the deformation of fibrous cellular skeleton caused by the dehydration and cyclization of PAA during the thermal annealing process. As a result, the density and porosity of all composite aerogel keeps almost constant at 13.38 mg cm^{-3} and 99%, respectively, which are not affected by the increasing CNTs content. All these demonstrates the compressive mechanical properties of composite aerogel can be effectively enhanced through increasing CNTs loading without sacrificing the lightweight porous architecture.

Subsequently, series of cyclic compression tests were conducted to explore the potential application of PIF/CNTs composite aerogel for pressure sensor. Figure 2D and S19 illustrates the stress-strain curves of all PIF/CNTs composite aerogels under stepwise cyclic compression, and the typical hysteresis loop is clearly seen in each compression cycle owing to the elastic porous fibrous structure. Meanwhile, two distinct stages are obviously observed during the loading process, including the linear elastic region of $0<\varepsilon<50\%$ within which the stress exhibits slow linear increase arising from elastic deformation of fibrous cellular skeleton, and the dentification region of $\varepsilon>50\%$ within which the stress increases sharply due to the contraction of porous structure. Importantly, the PIF/CNTs-0.5 can restore to its initial state even after being compressed to 90% strain without being crushed and endure a stress up to 200 kPa, the excellent compressibility, recoverability, and compression strength will undoubtly make the PIF/CNTs

composite aerogel to be ideal pressure sensor with wide working range. Furthermore, as depicted in Figure S20, owing to the regulation of partial unstable porous structure upon external compression, the typical hysteresis loops all PIF/CNTs composite aerogels reduce gradually in the initial compression cycles and then the stress-strain curves are almost coincided with each during the long-term cyclic compression process (50% strain, 1000 times). What's more, their corresponding statistical values of maximum stress, energy loss coefficient, and residual strain also tend to be stable after the initial stabilization process (Figure 2E and S21), exhibiting excellent fatigue resistance towards practical applications. Notably, smaller residual strain is observed for PIF/CNTs composite aerogel with higher CNTs loading, demonstrating the addition of CNTs is beneficial for enhancing the structural robustness and fatigue resistance based on its enhancement effect on the porous fibrous structure. Here, the residual strain of PIF/CNTs-0.5 is as low as 4.5%, which is superior to other polymeric foam [27] and fibrous foams [28].

Figure 2F presents the dynamic compressive viscoelastic properties of PIF/CNTs-0.5. In the wide temperature range from -50 to 300 °C, the nearly constant storage modulus and loss modulus indicate the good thermal stability. In addition, the damping ratio is as low as ~0.1 in the whole temperature range, verifying the outstanding elasticity with excellent harsh temperature tolerance. Besides, as shown in Figure 2G and Video S3, PIF/CNTs-0.5 can rebound a 10 g weight (~300 times its weight) and recover to its initial state at a recovery speed of~548 mm s^{-1}, which is much faster than the GO-cellular monolith (117 mm s^{-1}) [29], GO-coated CNTs aerogel (11.2 mm s^{-1}) [30], foamlike CNTs film (2 mm s^{-1}) [31], aligned CNTs array (1.6 mm s^{-1}) [32] and

CNTs sponge(1.2 mm s^{-1}) [33], and similar to the carbon–graphene monolith (580 mm s^{-1}) [34], and BC–PMSQ hybrid aerogel (567 mm s^{-1}) [14] (Figure 2H).

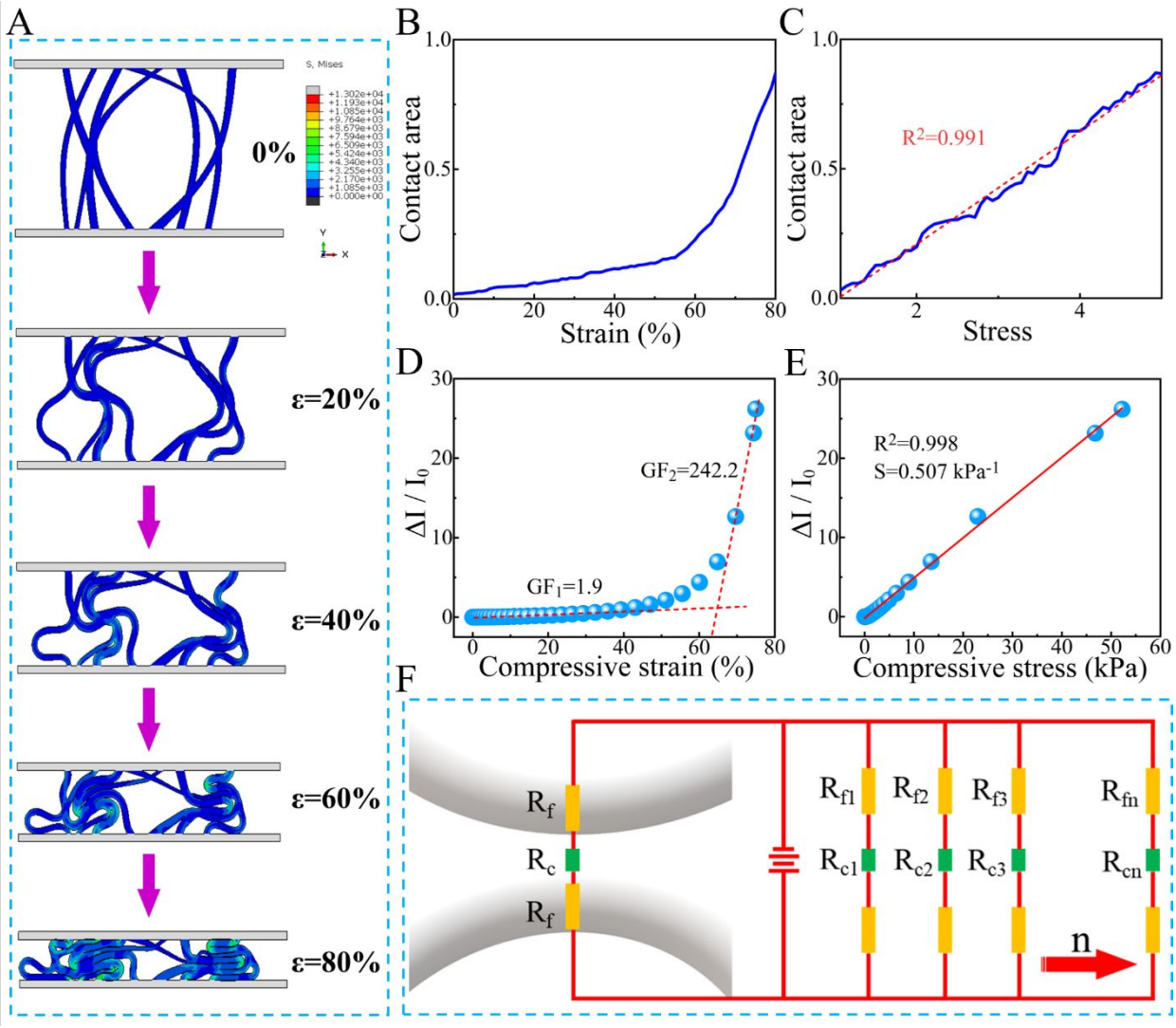

Figure 3. Pressure sensing and mechanism analysis of PIF/CNTs composite aerogel. (A) Finite element modeling of porous fibrous structure under different compression strains. The plots of the simulated contact area change as a function of (B) compression strain and (C) stress. Relative current variation versus (D) compression strain and (E) pressure. (F) Schematic diagram of a representative conductive path between aerogel fibers, and the corresponding equivalent circuit model.

Based on the outstanding porous fibrous skeleton, PIF/CNTs conductive composite aerogel was applied to the piezoresistive sensor. Generally, piezoresistive sensing mechanism of the

conductive composite aerogels can be explained by the change of contact area among conductive skeletons that results in the variation of electrical resistance, so their sensing performances can be seriously affected by the variation of contact mode during the compression process. The specific models of flexible and elastic conductive fibrous skeleton under different compression strains are simulated using nonlinear finite-element method simulation (Figure 3A), in which the fibrous skeleton deformation induced fiber contact is marked in green color. Clearly, compression induced bending deformation of flexible conductive fibrous skeleton leads to point contact between adjacent fibers in the initial elastic region (i.e., 20% and 40%), but the larger compression in the dentification region (i.e., 60% and 80%) can enable the formation of surface contact between adjacent fibers. As seen in Figure 3B, the simulated compression strain dependent contact area exhibits a slow linear growth in the initial elastic region, which could not construct additional effective conductive network significantly, causing subtle electrical signal variation and lower strain sensitivity. Then, the compression strain induced contact area increases rapidly in the following dentification region, enabling the formation of surface contact between adjacent fibers, thus resulting in much more new conductive paths and higher strain sensitivity. Interestingly, the corresponding pressure dependent contact area displays an excellent linear increasing behavior in the whole pressure range (Figure 3C), implying the sustainable and stable change of conductive paths and constant pressure sensitivity, which happens to be what we trying to achieve.

To verify the simulated results stated above, piezoresistive sensing performances of our

prepared PIF/CNTs composite aerogel were investigated. Figure 3D displays the relative current change ($\Delta I/I_0=(I-I_0)/I_0$, where I and I_0 represent the instantaneous current and initial current of composite aerogel, respectively) curve of the composite aerogel with increasing compression strain to 80%, in which a linear sensing region with a constant strain (ε) sensitivity (Gauge Factor, GF= $(I-I_0/ I_0)/\varepsilon$) of 1.9 followed by an exponential growth region with a GF up to 242.2 are clearly observed. Besides, the corresponding pressure sensing behavior was also explored (Figure 3E), and an excellent linear sensing mode with a constant pressure (P) sensitivity (Sensitivity, S= $(I-I_0/ I_0)/P$) as high as 0.507 kPa^{-1} is obtained in a wide working range (0.01–53.34 kPa). These results are in good consistent with the simulation prediction, suggesting that the construction of fibrous porous structure is good to achieve ideal linear pressure sensor, which is beneficial for easy readout during the signal processing.

Additionally, the resistance of prepared PIF/CNTs composite aerogel was also quantitatively analyzed. As shown in Figure 3F, the composite aerogel is composed of series of fiber pair, of which the resistance (R) is the sum of the intrinsic resistance of fiber (R_f) and the contact resistance between adjacent fibers (R_c), so the total resistance (R) of the sensor can be expressed as equation (1):

$$\frac{1}{R}=\sum_{i=1}^{n}\frac{1}{R_{fi}+R_{ci}+R_{fi}}=\frac{n}{R_c+2R_f} \quad (1)$$

Here, the intrinsic resistance of the fiber is much smaller than the contact resistance between adjacent fibers ($R_f \ll R_c$), so, Equation (1) can be is simplified as follows:

$$R=\frac{R_c}{n} \quad (2)$$

According to the Holm equation [35], R_c can be expressed as equation (3):

$$R_c = \frac{\rho d}{A_c} \tag{3}$$

Where ρ is the electrical conductivity of the fiber, d is the diameter of the fiber, A_c is the contact area that can be regarded as the integration of countless contact spots on a 2D plane.

Based on the contact mechanics theory proposed by Bush et al. [36], the relationship between compressive stress (P) and contact area can be given as equation (4):

$$A_c = k\frac{P}{E} \tag{4}$$

Where k is a constant and E is the modulus of elasticity. After substituting equations (3) and (4) into equation (2), R can be expressed as equation (5):

$$R = \frac{\rho dE}{kPn} \tag{5}$$

Therefore, the current signal (I) of the sensor at a certain voltage (U) could be written as:

$$I = \left(\frac{knU}{\rho dE}\right)P \tag{6}$$

It can be seen from equation (7) that the electrical signal is linearly related to pressure, demonstrating that the construction of porous fibrous structure is good to linear pressure sensing mode.

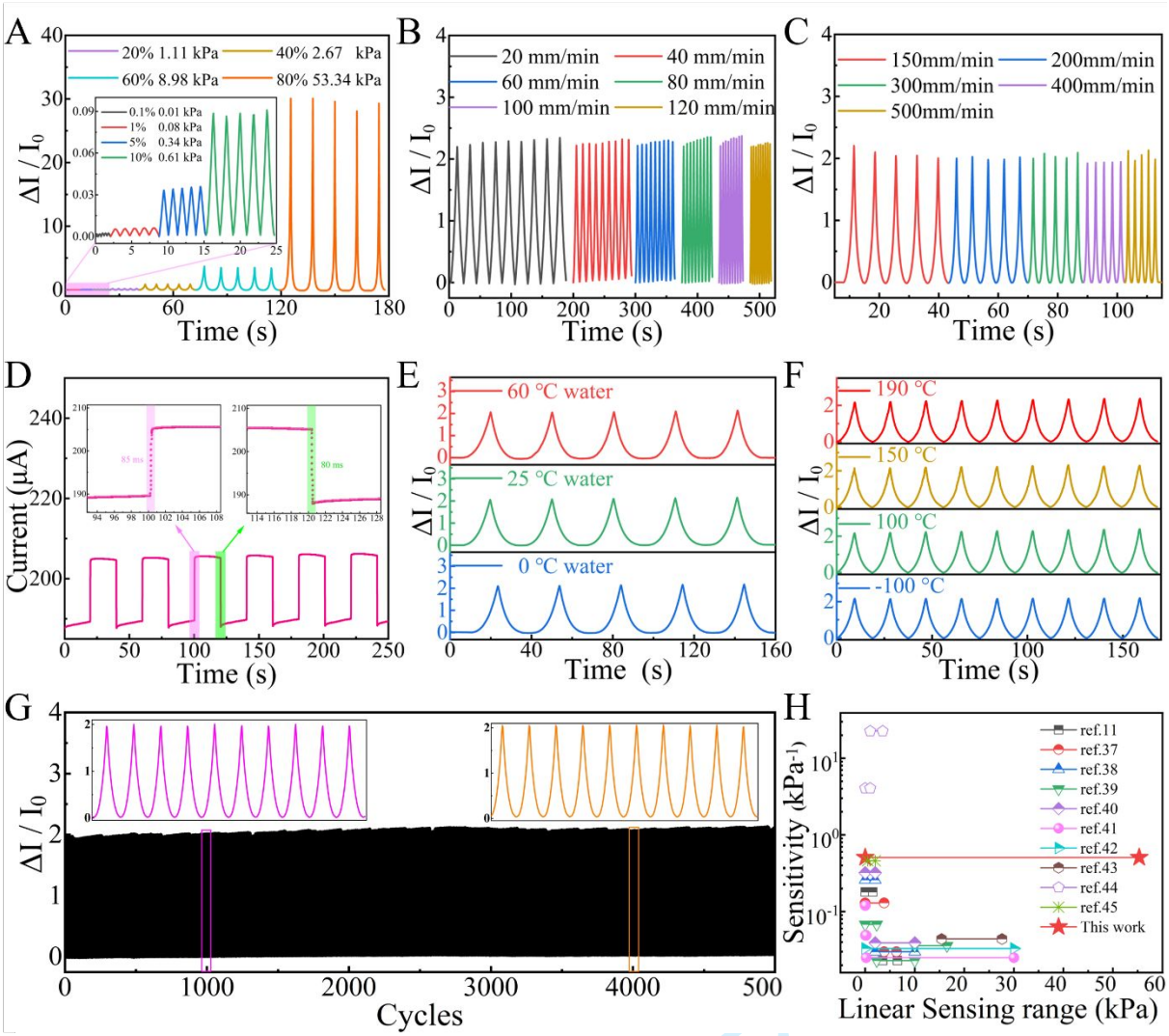

Figure 4. Pressure sensing performances of PIF/CNTs composite aerogel-based pressure sensor. Cyclic pressure sensing behavior of the sensor under (A) different pressure levels (20 mm/min) and (B&C) different compression rates at 50% strain. (D) Response/recovery time of the sensor at a compression rate of 500 mm/min and 1% strain. Cyclic pressure sensing behavior of the sensor in (E) water at different temperatures and (F) extreme temperature environments (-100 –190 ℃). (G) Cyclic sensing stability of the sensor over 5000 cycles at 50% strain. (H) Comparation of the working range and sensitivity of the sensor with other previously reported materials.

Figure 4A shows the relative current change of the PIF/CNTs composite aerogel-based pressure sensor upon progressive exerted compression. Clearly, the pressure sensor outputs stable and recoverable electrical current signal upon different pressure levels, and the sensitivity also increases with increasing pressure up to 53.34 kPa. It is worth noting that it can effectively detect

a pressure as low as 0.01 kPa, demonstrating an ultralow detection limit which is superior to that of human skin (100 Pa). Hence, our prepared composite aerogel-based pressure senor can be used for the detection of both subtle and high stress. In addition, the pressure sensor presents good rate independent pressure sensing property (Figure 4B and C), of which excellent cyclic pressure sensing behavior can be well maintained under different compression rates especially for ultra-high compression rates of 150–500 mm/min, enabling it to be applicable in high-speed operation system. What's more, a fast response time of 85 ms and recovery time of 80 ms were also obtained for the pressure sensor (Figure 4D). All these can be ascribed to the super resilience and good structural stability of the composite aerogel as shown Figure S22 and Video S4.

Considering the diverse working environments in practical application, environmental tolerance of the PIF/CNTs composite aerogel-based pressure sensor was further evaluated. Figure 4E illustrates the cyclic pressure response curve of the sensor immersed in water at different temperatures. It can be obviously observed that the response pattern keeps good stability without being affected by regardless of hot water or ice water, which can be ascribed to the hydrophobicity of polyimide matrix. Meanwhile, benefiting from the of excellent high and low temperature resistance of polyimide, the sensor also exhibits excellent sensing stability in harsh temperature environments such as -100, 100, 150, and 190 °C (Figure 4F), such a good extreme temperature tolerance makes it applicable in the fields of cold chain transportation, deep space exploration, national defense, and military. Finally, as presented in Figure 4G, long-term cyclic pressure sensing behavior of the sensor under 50% strain over 5000 cycles were performed,

where the stable and reproductive response pattern is well maintained, and no signal attenuation is observed in the whole testing process, demonstrating excellent fatigue resistance. Therefore, our prepared PIF/CNTs composite aerogel-based pressure sensor possesses excellent environmental tolerance, showing great superiority to other conventional polymer-based pressure sensor. More importantly, as illustrated in Figure 4H [11,37-43], our pressure sensor also displays higher sensitivity (0.507 kPa^{-1}) in a ultra-wider linear range (0.01-53.34 kPa) than that of Ppy/PDMS pressure sensor (0-2 kPa, 0.32 kPa^{-1}; 2-10 kPa, 0.039 kPa^{-1}), percolative Pd metal nanoparticle arrays pressure sensor ((0-0.05 kPa, 0.12 kPa^{-1}; 0.05-0.2 kPa, 0.049 kPa^{-1}; 0.2-30 kPa, 0.025 kPa^{-1}), and Ag/BTO/Ag pressure sensor (15.4-27.6 kPa, 0.044 kPa^{-1},).

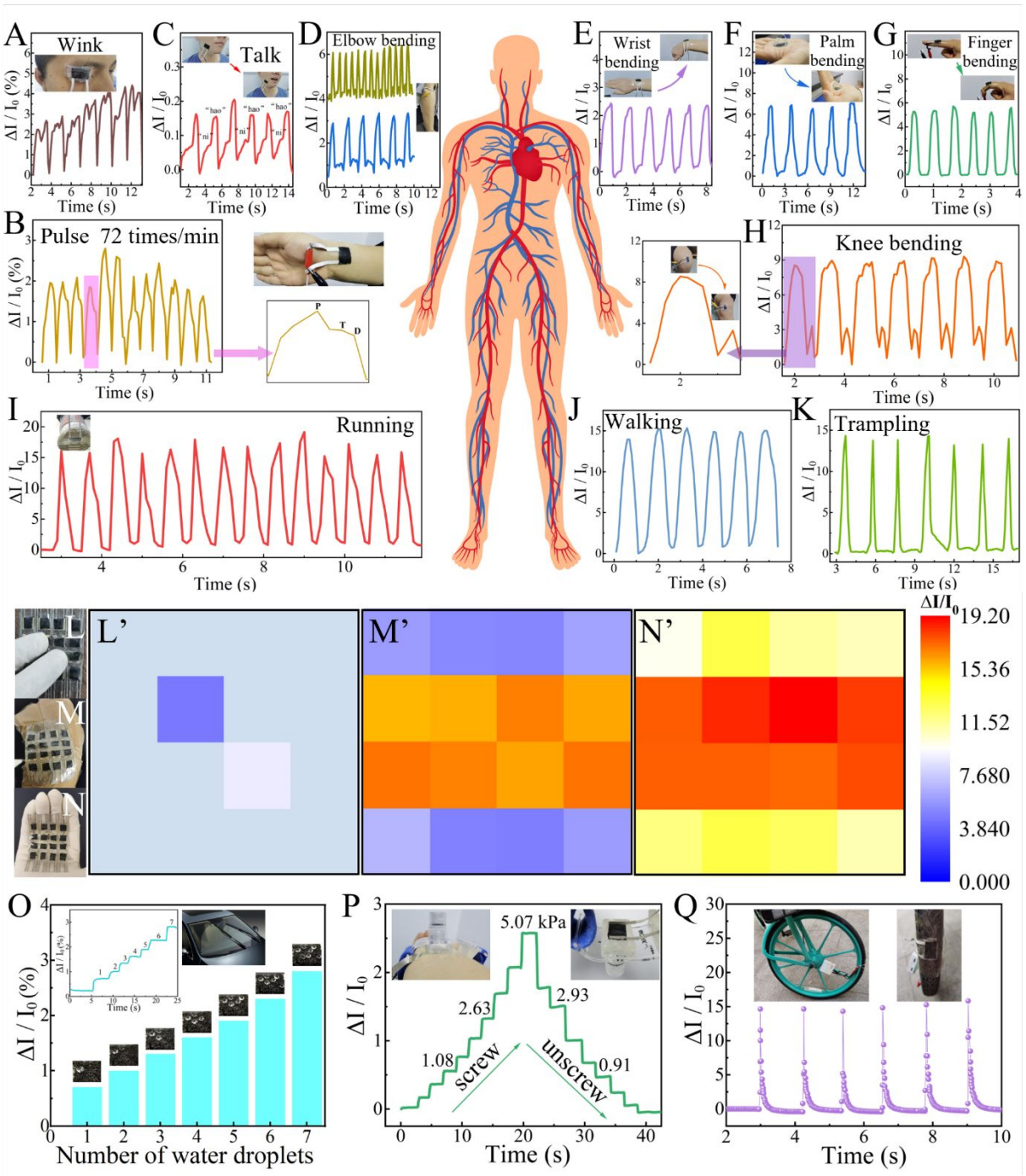

Figure 5. Real-time monitoring of physiological signal and human motion. (A) Blinking signal of eyelid variation monitored by sticking a sensor on the eyelid. (B) Pulse signal obtained from the sensor attached on the wrist. The right illustration is a complete radial artery pulse waveform, including "P", "T" and "D" peaks. (C) Pronunciation recognition through attaching the sensor to the volunteer's cheek to detect the facial muscle motion. (D) Elbow bending state detection using the attached sensor on the elbow. (E) Wrist bending detection by sticking the sensor to the wrist. (F) Detection of palm bending through the sensor sticked in the palm of volunteer's hand. (G) Detection of finger bending using the sensor fixed on volunteer's finger. (H) Knee

bending state monitoring based on the fixed sensor on volunteer's knee. Detection of (I) running, (J) walking, and (K) trampling by fixing the sensor to the sole of the shoe. (L&L') Discrimination of different finger location and pressure based on the current variation intensity of different sensing units of the assembled E-skin. Skin stress distribution detection of (M) wrist and (N) palm based on their corresponding current variation mapping (M'&N') using the assembled E-skin. (O) Monitoring the simulated different raindrops amount to display the potential of the pressure sensor in controlling the automobile automatic wiper. (P) Pressure sensor fixed to the hemostatic device to display the exerted pressure. (Q) Recording the riding speed using the pressure sensor fixed to the bicycle wheel.

Subsequently, due to the conformal ability, ultralow detection limit, and wide working range of the composite aerogel-based pressure sensor, real-time monitoring of subtle physiological signal and intense human motion were conducted by fixing the sensor on different human body parts with the help of medical tape. In modern medicine, fast and accurate physiological signal monitoring has an important clinical significance. Blinking can intuitively transmit human mood and is also an effective channel to monitor the state of long-term coma patient. Obviously, the pressure sensor attached on the eyelids can generate regular current signal towards human blinking (Figure 5A). In addition, subtle pulse signal is an important data for evaluating human health condition and can be detected by sticking the sensor on the volunteers' wrists, where the pulse rate can be determined to be 66 beats per minute based on the regular and stable radial artery pulse signal within 10 seconds (Figure 5B). Meanwhile, subtle characteristic peaks of "P" (percussion wave), "T" (tidal wave) and "D" (diastolic wave) of pulse waveform can also been effectively distinguished. To detect the facial muscle motion, the sensor was placed on the volunteer's cheek that could output stable and repeatable current signal towards speaking, and the different pronunciations can also produce signals with different intensities, showing good voice recognition (Figure 5C).

Aside from the detection of tiny physiology signal, the movement of different human body joints can also be effectively monitored. As shown in Figure 5D, elbow motion with different bending angles can be easily captured and distinguished according to the different current response intensity. Here, a larger bending angle can generate higher pressure that cause greater electrical signal change. Meanwhile, reproducible and stable sensing signals can also be successfully detected for other similar human body motions including wrist bending (Figure 5E), palm bending (Figure 5F), finger bending (Figure 5G) and knee bending (Figure 5H) through adhering the sensor on their corresponding joints. What's more, the sensor is also fixed to the sole of the shoe to monitor the moving state, where the states of running (Figure 5I), walking (Figure 5J), and trampling (Figure 5K) are clearly distinguished based on the frequency of the sensing signal. As a result, the good recognition for body joint movement endows it with great potential in advanced limb exoskeleton system based the muscle tension and joint force signal for rehabilitation therapy.

Some other potential applications of the prepared composite aerogel-based pressure were further explored. As seen in Figure 5L and L', when two fingers press the assembled E-skin with a 4×4 pressure sensor array, two separated sensing unit outputs different current variation signal due to the different finger pressure, demonstrating the excellent discrimination for the finger location and pressure. What's more, the assembled E-skin also has good conformability with the human body parts of wrist (Figure 5M) and palm (Figure 5N), and their skin spatial stress distribution under bending state can be easily and precisely recorded based on the skin

deformation induced current variation (Figure 5M' and N'). All these indicate that our prepared pressure sensor is a promising product for flexible wearable electronic devices.

Figure 5O shows the sensing performance of the sensor towards increasing water drop number, and the current variation intensity exhibits an increasing trend due to the accumulated impact effect of the falling water drop. Hence, it can be applied as a sensing unit to control the start and working frequency of automobile automatic wiper based on the calculated water drop. Medical hemostatic devices can cause the discomfortability of patients because of the unmeasurable pressure. To solve this problem, as shown in Figure 5P, the sensor was fixed onto the hemostatic devices to provide assistant identification of practical pressure. As expected, the pressure at different stages during the screwing and loosening process can be accurately detected, providing an effective basis for the degree of screwing. Excellent pressure sensors can not only monitor tiny/small stress, but also need to have stable and accurate recognition for large stress. As a proof of this concept, the pressure sensor connected with a Bluetooth transmission device was fixed to the bicycle wheel. Clearly, it can be observed obviously from Figure 5Q and Video S5 that the sensor can generate sharp response signal when the bicycle with an adult rider (80 Kg) rolls on the sensor. Meanwhile, the response pattern can also keep good stability and reproductivity during the continuous cycling, which can be ascribed to the robust and superelastic porous fibrous structure. As a result, the riding speed can be easily recorded based on the number of response peak in a certain time, supplying reference basis for daily training of athletes. In a word, our prepared PIF/CNTs composite aerogel-based pressure sensor possesses broad application

areas, including human health monitoring, artificial intelligence, intelligence control, and physical training.

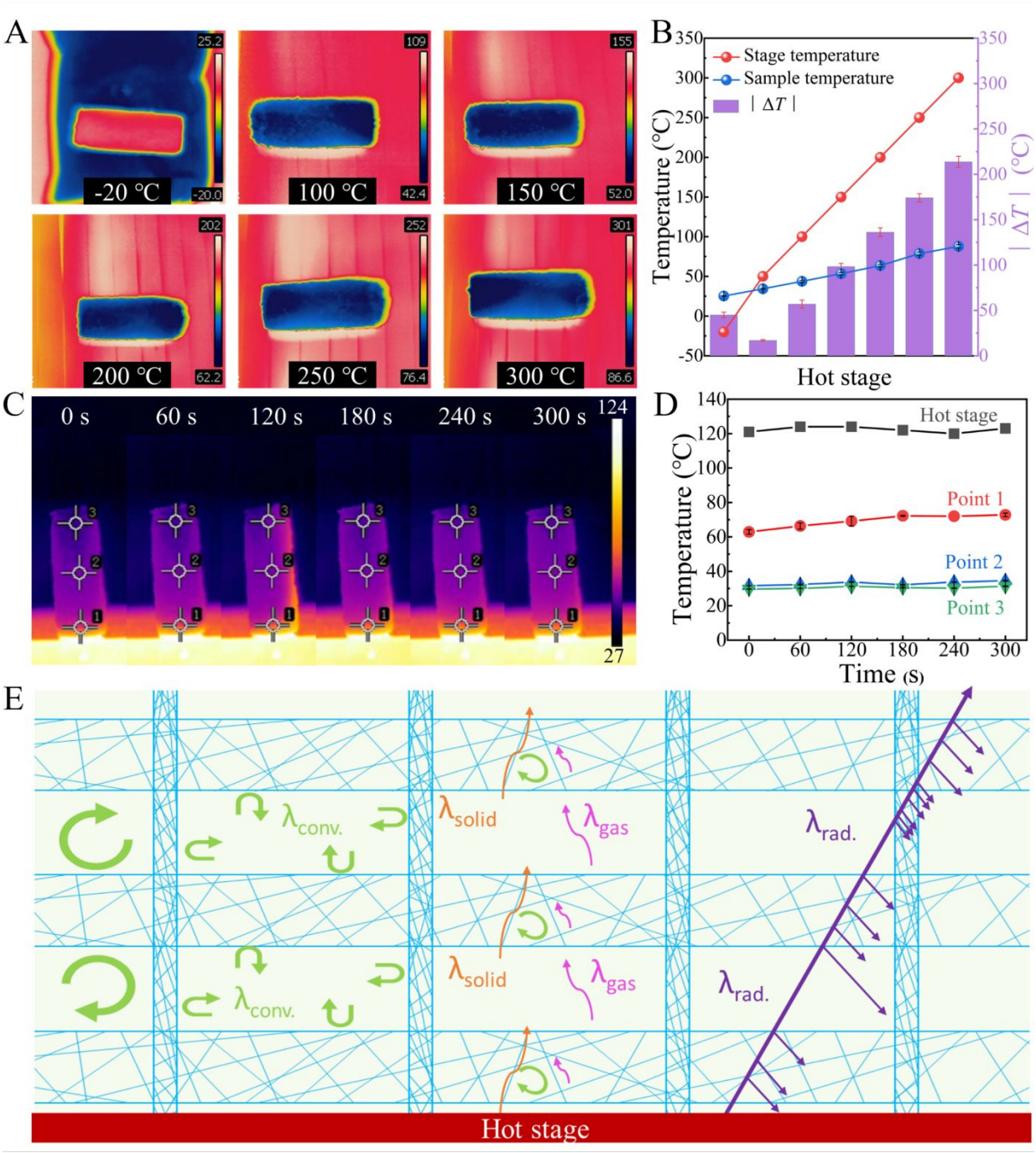

Figure 6. Thermal insulation performance of PIF/CNTs composite aerogel. (A) Infrared images of the composite aerogel placed on a stage with different temperatures after 5 minutes stabilization. (B) Aerogel upper surface temperature and its temperature difference (ΔT) compared with hot stage based on the infrared images.

(C) Infrared images of the composite aerogel placed on a 120 °C stage and (D) the corresponding temperature change of the bottom, middle and upper part at an interval of 60 second. (E) Schematic illustration of the thermal insulation mechanism of the composite aerogel.

Due to the spider web-like porous structure and a porosity of higher than 99%, PIF/CNTs composite aerogel is expected to be thermal insulative to protect the skin from extreme environmental temperature when served as a wearable pressure sensor. Figure 6A presents the infrared images of the composite aerogel placed on a stage with different temperatures ranging from -20 °C to 300 °C, where the aerogel surface displays a significant color difference compared with that of stage surface after 5 minutes stabilization, showing the expected thermal insulation property. Meanwhile, their detail surface temperatures were extracted based on the color of infrared images, and the corresponding absolute temperature difference ($|\Delta T|$= |stage temperature-sample temperature|) were calculated and plotted in Figure 6B. Clearly, aerogel surface temperature varies slightly from 25 °C and 87 °C when the stage temperature increases from -20 °C to 300 °C, and higher $|\Delta T|$ is obtained for the aerogel placed on the stage with more significant difference with the ambient temperature (30 °C). Specifically, the aerogel surface temperature is only 87 °C, and the $|\Delta T|$ reaches 214 °C when the stage temperature is up to 300 °C. Meanwhile, the aerogel surface temperature is also close to the ambient temperature even the stage temperature is as low as -20 °C. what's more, the thermal conductivity of the prepared composite aerogel was measured to be 0.032 W m^{-1} K^{-1} under room temperature. All these indicate that our prepared composite aerogel possesses permanent thermal insulation property under a wide temperature range, enabling it workable in both normal and harsh environments.

Furthermore, the thermal insulation stability of the composite aerogel under a temperature of

120 °C was investigated through monitoring the temperature changes in different sites. As shown in Figure 6C, the overall infrared image color in an interval of 60 seconds shows almost no obvious change in a period of 300 seconds, and the extracted temperature in different sites are plotted in Figure 6D, where the temperature of the lower part with a heigh of only 2 mm (Point 1) increases by 11 °C but $|\Delta T|$ is still as high as 48 °C, demonstrating a strong thermal insulation property. As for the middle and upper part, the temperature of them keeps almost stable at 30 °C and 33 °C, respectively, which are almost the same as the ambient temperature. Hence, a complete thermal insulation can be achieved through tunning the effective aerogel thickness.

Such an excellent thermal insulation property can be explained by the schematic diagram of the heat transfer process shown in Figure 6E, in which the solid thermal conduction (λ_{solid}), air thermal conduction (λ_{air}), heat convection ($\lambda_{conv.}$), and heat radiation ($\lambda_{rad.}$) contribute to the thermal conductivity. Here, ultrahigh porosity (99%) of composite aerogel is beneficial for a significant reduction in overall thermal conduction because λ_{air} is far lower than λ_{solid}, and air molecule can also be confined in the sub-micrometer pores in the spider web-like skeleton, resulting in an attenuation of heat convection to some extent. More importantly, the spider web-like skeleton is regarded to be favorable for stronger multiple infrared light reflection inside the aerogel compared with that of solid cellular skeleton, resulting in weaker heat radiation. As a result, the special spider web-like structure is conductive for the outstanding thermal insulation of wearable pressure sensor applied in harsh environmental temperature, enabling it to be applicable in ongoing and near-future aerospace exploration.

4.Conclusions

We have successfully developed a robust and superelastic PIF/CNTs composite aerogel-based pressure sensor with linear response, ultralow detection limit, and high sensitivity in a wide sensing range. Triethylamine was innovatively applied to achieve homogeneous dispersion of PIF in CNTs aqueous dispersion, and water soluble PAA was adopted as a glue to weld PIF-PIF and PIF-CNTs strongly via a thermal imidization process. The constructed hierarchical porous fibrous structure enables a significant linear variation in the contact area between adjacent conductive fiber in response to applied pressure. Given the outstanding property of composite aerogel and special porous fibrous network, the prepared sensor displays outstanding linear sensing mode with ultralow detection limit (10 Pa), high sensitivity (0.507 kPa^{-1}) in the pressure range of 0.01–53.34 kPa, fast response/recovery time (85/80 ms), stable high compression rate response (as high as 500 mm/min), and excellent fatigue resistance over 5000 times cyclic compression. We have also confirmed the potential application of the sensor from the monitoring of human physiology and motion signal to intelligence control. Importantly, the good extreme temperature tolerance and thermal insulation property of the composite aerogel will also provide new opportunities for emerging applications such as the sensing unit of space suit and inflatable structures of lunar/mars habitat.

Acknowledgments: The research was financially supported by National Natural Science Foundation of China (NO: 12072325, 52125205, U20A20166 and 52192614), National Key R&D Program of China (2019YFA0706802, 2021YFB3200304 and 2021YFB3200302), the 111

project (D18023), Natural Science Foundation of Beijing Municipality (Z180011 and 2222088), Shenzhen Science and Technology Program (Grant No. KQTD20170810105439418) and the Fundamental Research Funds for the Central Universities.

Author contributions: Wenke Yang, Hu Liu and Chuntai Liu performed the experiments, analyzed the data, and co-wrote the manuscript. Hu Liu, Pan Caofeng and Changyu Shen conceived and modified the work. Houyi Du assisted with the sensing measurements. Chunfeng Wang and Rui Yin assisted with the grammar modification. Zhang Minyue assisted with the real-time sensing monitoring. All authors have given approval to the final version of the manuscript.

Conflict of interest: The authors declare that they have no conflict of interest.

Supplementary information: Experimental details are available in the online version of the paper.

References

[1] Zhou B, Liu Z, Li C, et al. A highly stretchable and sensitive strain sensor based on dopamine modified electrospun sebs fibers and mwcnts with carboxylation. Adv Electron Mater, 2021, 7: 2100233

[2] Lai YC, Deng J, Niu S, et al. Electric eel - skin - inspired mechanically durable and super - stretchable nanogenerator for deformable power source and fully autonomous conformable electronic - skin applications. Adv Mater, 2016, 28: 10024

[3] Xu M, Cai H, Liu Z, et al. Breathable, degradable piezoresistive skin sensor based on a sandwich structure for high-performance pressure detection. Adv Electron Mater, 2021, 7: 2100368

[4] Wang H, Li S, Wang Y, et al. Bioinspired fluffy fabric with in situ grown carbon nanotubes for ultrasensitive wearable airflow sensor. Adv Mater, 2020, 32: 1908214

[5] Waqar M, Wu H, Chen J, et al. Evolution from lead-based to lead-free piezoelectrics: Engineering of lattices, domains, boundaries, and defects leading to giant response. Adv Mater, 2022, 34: 2106845

[6] Fan F-R, Tian Z-Q, Wang ZL. Flexible triboelectric generator! Nano Energy, 2012, 1: 328-334

[7] Zhang Z, Gui X, Hu Q, et al. Highly sensitive capacitive pressure sensor based on a micropyramid array for health and motion monitoring. Adv Electron Mater, 2021, 7: 2100174

[8] Luo N, Huang Y, Liu J, et al. Hollow-structured graphene–silicone-composite-based piezoresistive sensors: Decoupled property tuning and bending reliability. Adv Mater, 2017, 29: 1702675

[9] Ma Y, Yue Y, Zhang H, et al. 3d synergistical mxene/reduced graphene oxide aerogel for a piezoresistive sensor. Acs Nano, 2018, 12: 3209-3216

[10] Alsharari M, Chen B, Shu W. Sacrificial 3d printing of highly porous, soft pressure sensors. Adv Electron Mater, 2022, 8: 2100597

[11] Qin Y, Peng Q, Ding Y, et al. Lightweight, superelastic, and mechanically flexible graphene/polyimide nanocomposite foam for strain sensor application. ACS Nano, 2015, 9: 8933-8941

[12] Kang S, Lee J, Lee S, et al. Highly sensitive pressure sensor based on bioinspired porous structure for real-time tactile sensing. Adv Electron Mater, 2016, 2: 1600356

[13] Cao X, Zhang J, Chen S, et al. 1d/2d nanomaterials synergistic, compressible, and response rapidly 3d graphene aerogel for piezoresistive sensor. Adv Funct Mater, 2020, 30: 2003618

[14] Zhang J, Cheng Y, Xu C, et al. Hierarchical interface engineering for advanced nanocellulosic hybrid aerogels with high compressibility and multifunctionality. Adv Funct Mater, 2021, 31: 2009349

[15] Liu H, Chen X, Zheng Y, et al. Lightweight, superelastic, and hydrophobic polyimide nanofiber /mxene composite aerogel for wearable piezoresistive sensor and oil/water separation applications. Adv Funct Mater, 2021, 31: 2008006

[16] Teo N, Jana SC. Solvent effects on tuning pore structures in polyimide aerogels. Langmuir, 2018, 34: 8581-8590

[17] Chen X, Liu H, Zheng Y, et al. Highly compressible and robust polyimide/carbon nanotube composite aerogel for high-performance wearable pressure sensor. ACS Appl Mater Inter, 2019, 11: 42594-42606

[18] Ren R-P, Wang Z, Ren J, et al. Highly compressible polyimide/graphene aerogel for efficient oil/water separation. J Mater Sci, 2019, 54: 5918-5926

[19] Yan L, Fu L, Chen Y, et al. Improved thermal stability and flame resistance of flexible polyimide foams by vermiculite reinforcement. J Appl Polym Sci, 2017, 134: 44828

[20] Chen ST, Jang MK, Wang KT. Facile amide bond formation from esters of amino-acids and peptides catalyzed by alkaline protease in anhydrous tert-butyl alcohol using ammonium-chloride triethylamine as a source of nucleophilic ammonia. Synthesis-Stuttgart, 1993, 858-860

[21] Zhang F, Feng Y, Qin M, et al. Stress controllability in thermal and electrical conductivity of 3d elastic graphene-crosslinked carbon nanotube sponge/polyimide nanocomposite. Adv Funct Mater, 2019, 29: 1901383

[22] Ashraf AR, Akhter Z, Simon LC, et al. Polyimide derivatives of 4,4′-bis((4-aminophenoxy)methyl)-1,1′-biphenyl: Synthesis, spectroscopic characterization, single crystal xrd and thermal studies. J Mol Struct, 2018, 1169: 46-58

[23] Wang S, Jiang SP, White TJ, et al. Electrocatalytic activity and interconnectivity of pt nanoparticles on multiwalled carbon nanotubes for fuel cells. J Phys Chem C., 2009, 113: 18935-18945

[24] Huang J, Wang J, Yang Z, et al. High-performance graphene sponges reinforced with polyimide for room-temperature piezoresistive sensing. ACS Appl Mater Inter, 2018, 10: 8180-8189

[25] Wang J, Liu D, Li Q, et al. Lightweight, superelastic yet thermoconductive boron nitride nanocomposite aerogel for thermal energy regulation. ACS Nano, 2019, 13: 7860-7870

[26] Fan W, Zhang X, Zhang Y, et al. Lightweight, strong, and super-thermal insulating polyimide composite aerogels under high temperature. Compos Sci and Technol, 2019, 173: 47-52

[27] Sun H, Xu Z, Gao C. Multifunctional, ultra-flyweight, synergistically assembled carbon aerogels. Adv Mater, 2013, 25: 2554-2560

[28] Liang H-W, Guan Q-F, Chen L-F, et al. Macroscopic-scale template synthesis of robust carbonaceous nanofiber hydrogels and aerogels and their applications. Angew Chem Int Edit, 2012, 51: 5101-5105
[29] Qiu L, Liu JZ, Chang SLY, et al. Biomimetic superelastic graphene-based cellular monoliths. Nat Commun, 2012, 3: 1241
[30] Kim KH, Oh Y, Islam MF. Graphene coating makes carbon nanotube aerogels superelastic and resistant to fatigue. Nat Nanotechnol, 2012, 7: 562-566
[31] Cao A, Dickrell P, Sawyer W, et al. Super-compressible foamlike carbon nanotube films. Science, 2005, 310: 1307-1310
[32] Suhr J, Victor P, Ci L, et al. Fatigue resistance of aligned carbon nanotube arrays under cyclic compression. Nature Nanotechnol, 2007, 2: 417-421
[33] Gui X, Wei J, Wang K, et al. Carbon nanotube sponges. Adv Mater, 2010, 22: 617-621
[34] Gao H-L, Zhu Y-B, Mao L-B, et al. Super-elastic and fatigue resistant carbon material with lamellar multi-arch microstructure. Nat Commun, 2016, 7: 12920
[35] Holm R. Electric contacts：theory and application. Springer-Verlag Berlin Heidelberg, 1967
[36] Bush AW, Gibson RD, Thomas TR. The elastic contact of a rough surface. Wear, 1975, 35: 87-111
[37] Mu C, Song Y, Huang W, et al. Flexible normal-tangential force sensor with opposite resistance responding for highly sensitive artificial skin. Adv Funct Mater, 2018, 28: 1707503
[38] Yao H-B, Ge J, Wang C-F, et al. A flexible and highly pressure-sensitive graphene–polyurethane sponge based on fractured microstructure design. Adv Mater, 2013, 25: 6692-6698
[39] Wu X, Han Y, Zhang X, et al. Large-area compliant, low-cost, and versatile pressure-sensing platform based on microcrack-designed carbon black@polyurethane sponge for human–machine interfacing. Adv Funct Mater, 2016, 26: 6246-6256
[40] Lee G-H, Park J-K, Byun J, et al. Parallel signal processing of a wireless pressure-sensing platform combined with machine-learning-based cognition, inspired by the human somatosensory system. Adv Mater, 2020, 32: 1906269
[41] Chen J, Zhang J, Hu J, et al. Ultrafast-response/recovery flexible piezoresistive sensors with DNA-like double helix yarns for epidermal pulse monitoring. Adv Mater, 2022, 34: 2104313
[42] Chen M, Luo W, Xu Z, et al. An ultrahigh resolution pressure sensor based on percolative metal nanoparticle arrays. Nat Commun, 2019, 10: 4024
[43] Song K, Zhao R, Wang ZL, et al. Conjuncted pyro-piezoelectric effect for self-powered simultaneous temperature and pressure sensing. Adv Mater, 2019, 31: 1902831
[44] Ma Y, Yue Y, Zhang H, et al. 3d synergistical mxene/reduced graphene oxide aerogel for a piezoresistive sensor. ACS Nano, 2018, 12: 3209-3216
[45] Yang C, Liu W, Liu N, et al. Graphene aerogel broken to fragments for a piezoresistive pressure sensor with a higher sensitivity. ACS Appl Mater Inter, 2019, 11: 33165-33172

Supporting Information

Robust and Superelastic Spider Web-Like Polyimide Fiber Based Conductive Composite Aerogel for Extreme Temperature Tolerant Linear Pressure Sensor

Wenke Yang,[1,2] Hu Liu,[1,2*] Houyi Du,[1] Minyue Zhang,[1] Chunfeng Wang,[3] Rui Yin,[1,4]

Caofeng Pan,[2*] Chuntai Liu,[1*] Changyu Shen[1]

[1]Key Laboratory of Materials Processing and Mold (Zhengzhou University), Ministry of Education; National Engineering Research Center for Advanced Polymer Processing Technology, Zhengzhou University, Zhengzhou, Henan 450002, China

[2]CAS Center for Excellence in Nanoscience, Beijing Key Laboratory of Micro-nano Energy and Sensor, eenennstitute of Nanoenergy and Nanosystems, Chinese Academy of Sciences, Beijing 101400, China

[3]College of Physics and Optoelectronic Engineering, Shenzhen University, Shenzhen 518060, China

[4]China Astronaut Research and Training Center, Beijing 100094, China

*: *Correspondence authors*

E-mail addresses: liuhu@zzu.edu.cn (H. L.); cfpan@binn.cas.cn (C. P.); ctliu@zzu.edu.cn (C. L.)

Table S1. Formulations of pure PIF aerogel

	PIF-0.3	PIF-0.5	PIF-1	PIF-1.5
PAA (mg)	60	100	200	300
PIF (mg)	200	200	200	200
TEA (mL）	40	40	40	40

Table S2. Formulations of PIF/CNTs composite aerogel

	PIF/CNTs-0.2	PIF/CNTs-0.3	PIF/CNTs-0.4	PIF/CNTs-0.5
CNTs (mg)	40	60	80	100
PAA (mg)	100	100	100	100
PIF (mg)	200	200	200	200
TEA (mL)	40	40	40	40

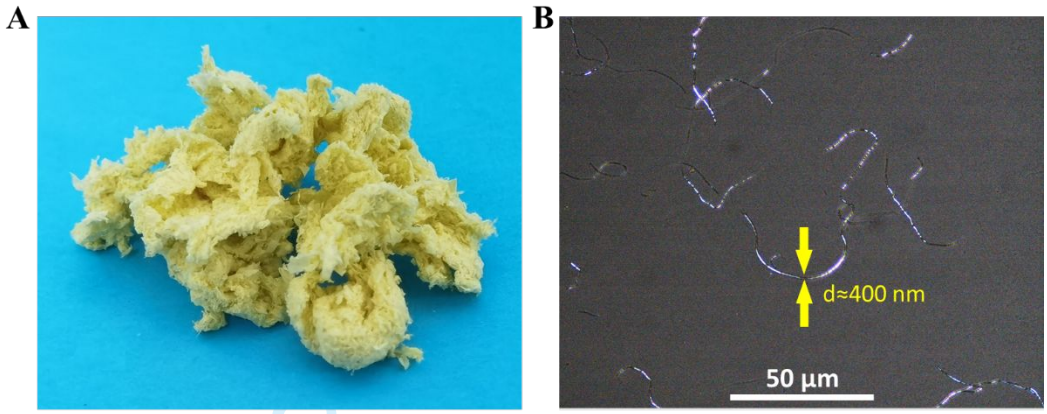

Figure S1. (A) Digital photo and (B) polarized microscope image of PIF.

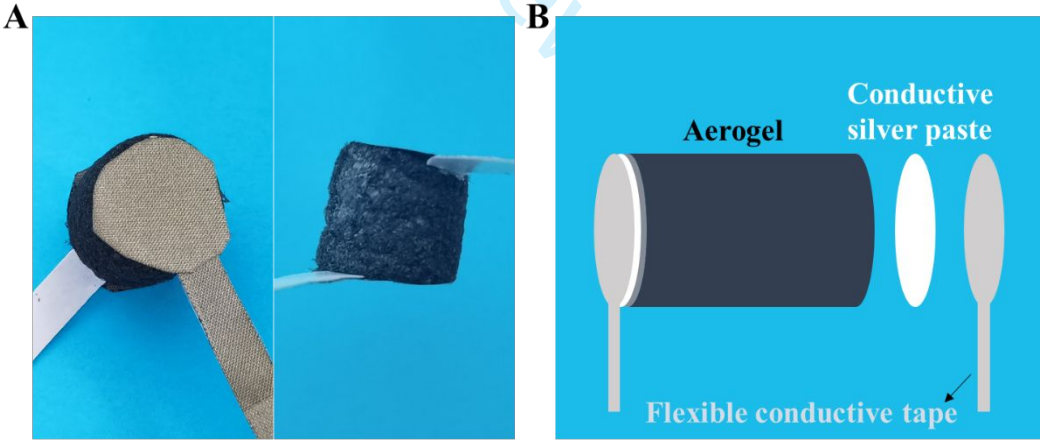

Figure S2. (A) Digital photo of the fabricated PIF/CNTs composite aerogel-based pressure sensor and (B) the corresponding structure diagram.

Figure S3. Home-made online pressure sensing test system

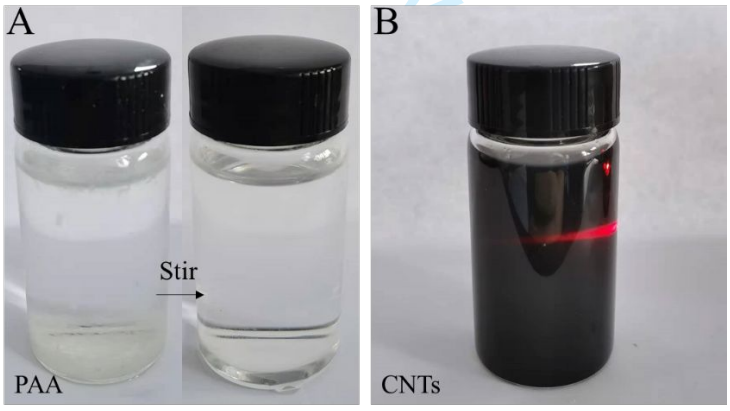

Figure S4. Excellent solubility and dispersibility of (A) PAA and (B) CNTs in water (Tyndall effect).

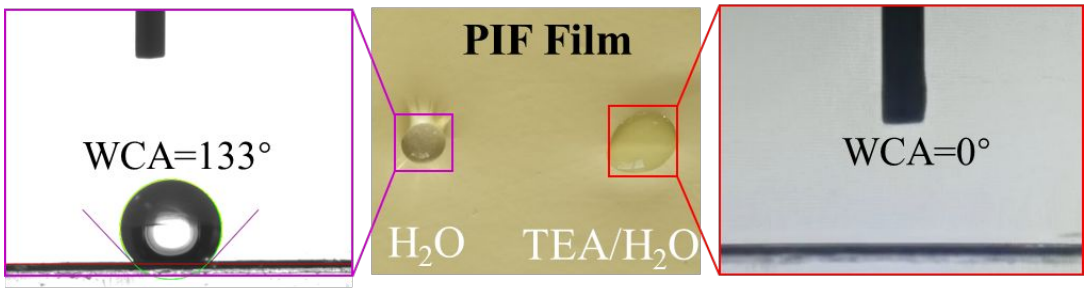

Figure S5. Optical photograph and corresponding WCAs of water droplets and TEA/H_2O droplets on the PI fibrous film.

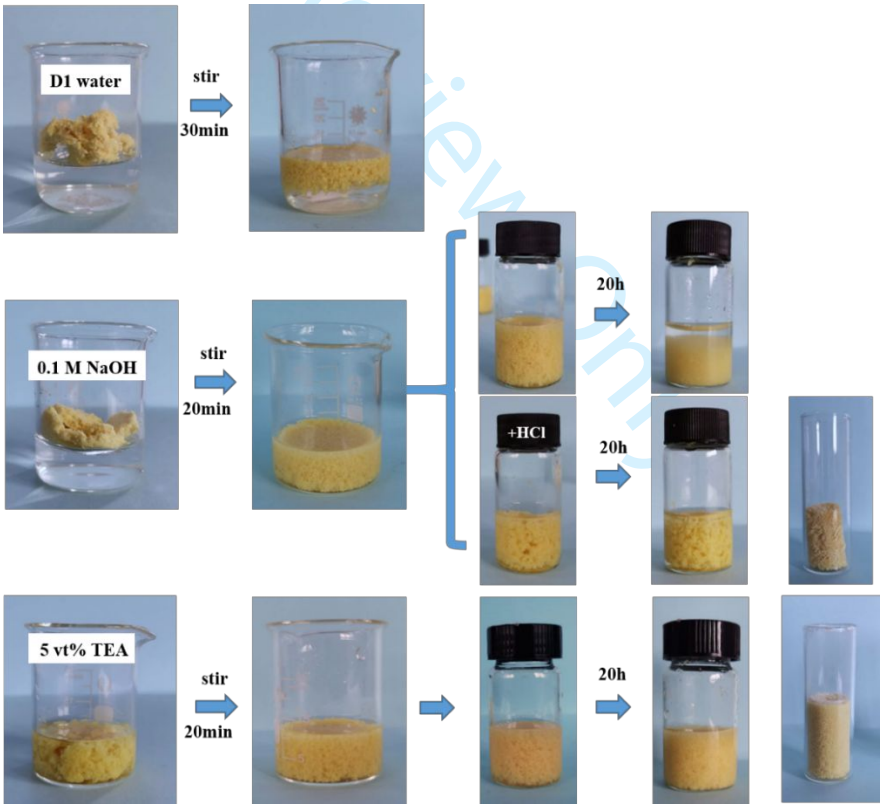

Figure S6. Digital photos showing the dispersibility of PIF in deionized water, 0.1 M NaOH solution and 5% TEA solution.

As shown in Figure S6, PIF has poor dispersibility in pure water, and all the fibers gather on the water surface. As for the NaOH solution, PIF can be well dispersed in water after stirring for 20 minutes, but the PIF can be destructed by the strong alkaline NaOH after 20 h, which is harmful for the mechanical property of the final products. Although the destruction can be timely blocked by adding HCl, the structure of the composite aerogel is still not good enough based on the aerogel surface. However, the weak alkaline TEA is good for the long-term homogeneous dispersion of PIF and homogeneous porous structure without deteriorating PIF.

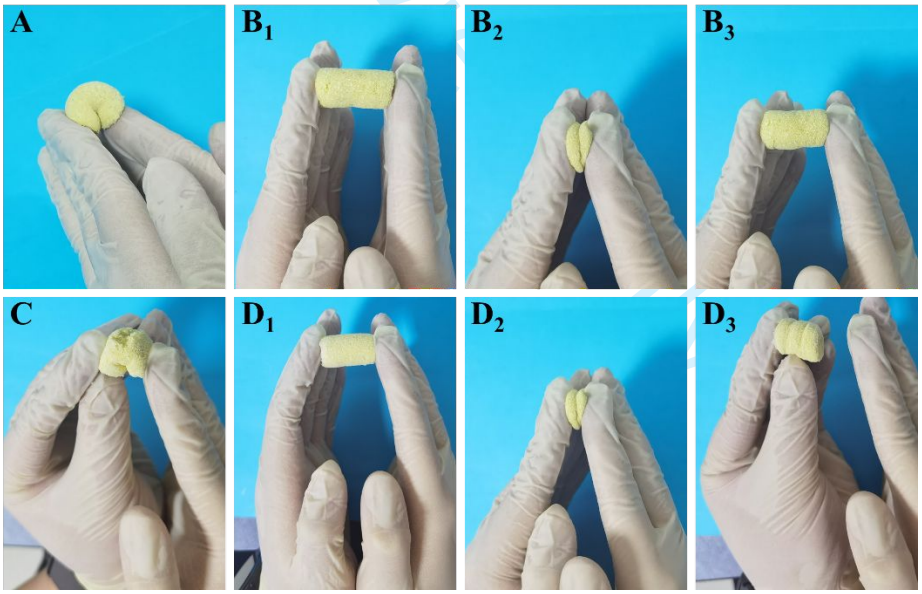

Figure S7. Digital photos showing the (A, C) bendability and (B_1-B_3, D_1-D_3) compressibility of PIF aerogel. Upper row: PIF aerogel with PAA; Lower row: PIF aerogel without PAA.

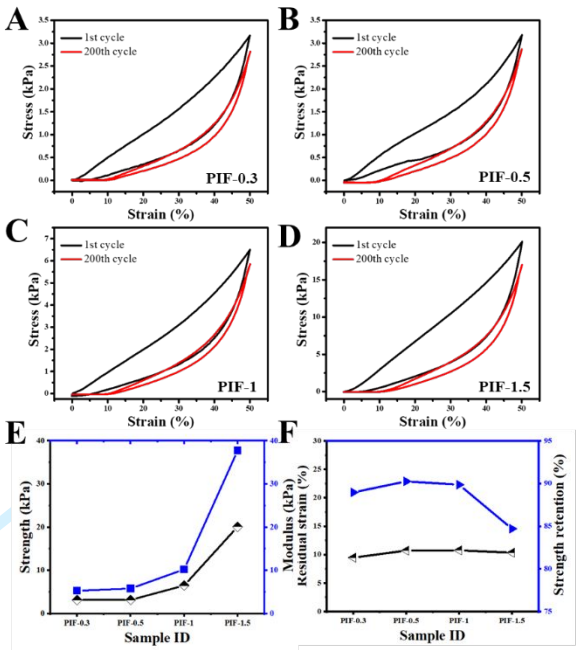

Figure S8. (A-D) Cyclic stress-strain curves of pure PIF aerogels with different PAA content. (E) Strength and modulus, (F) residual strain and strength retention of pure PIF aerogels with different PAA content.

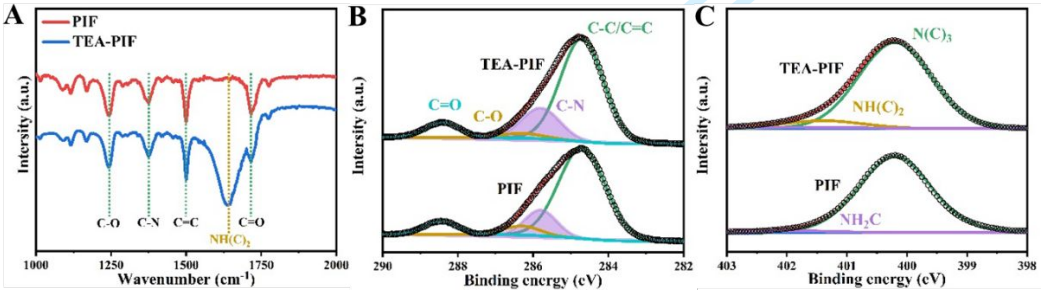

Figure S9. (A) FT-IR spectra and High-resolution XPS spectra of (B) C1s and (C) N1s of original PIF and PIF after being immersed in TEA aqueous solution (TEA-PIF).

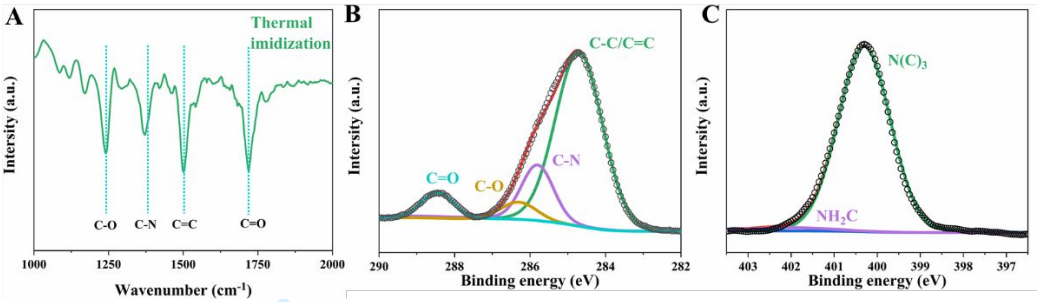

Figure S10. FT-IR spectra (A) and High-resolution XPS spectra of (B) C1s and (C) N1s of PIF after thermal imidization.

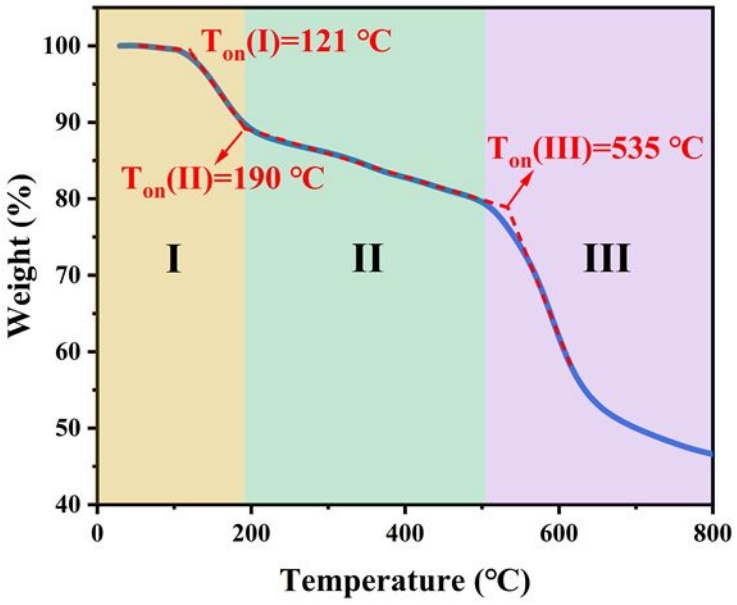

Figure S11. TG curve of PIF aerogel without thermal imidization in nitrogen atmosphere.

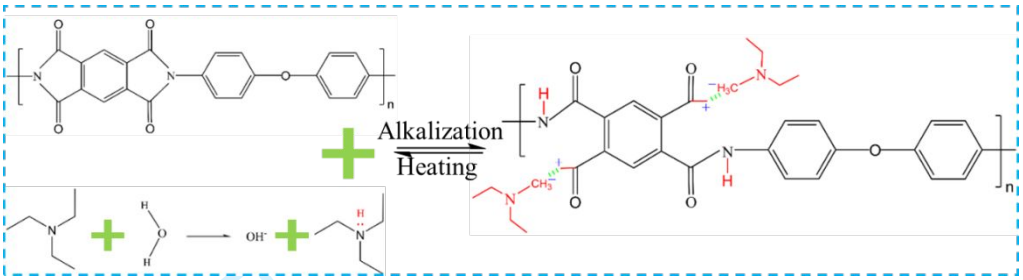

Figure S12. Dispersion mechanism of PIF in TEA aqueous solution.

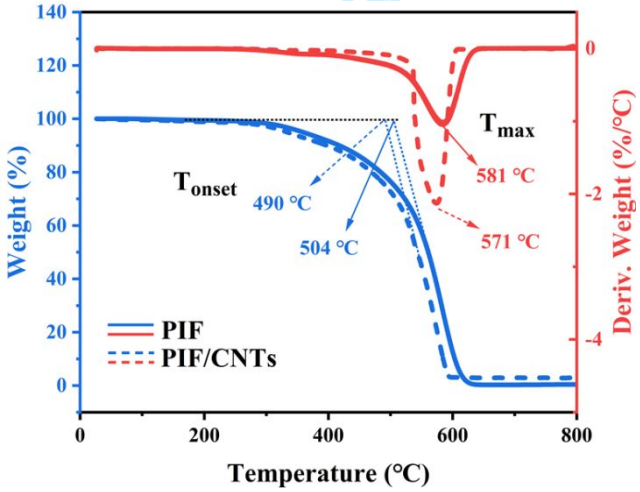

Figure S13. TG and DTG curves of pure PIF aerogel and PIF/CNTs composite aerogel.

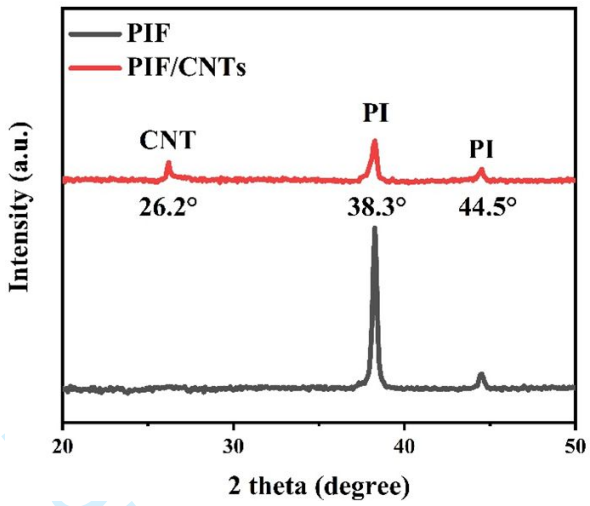

Figure S14. XRD patterns of pure PIF aerogel and PIF/CNTs composite aerogel.

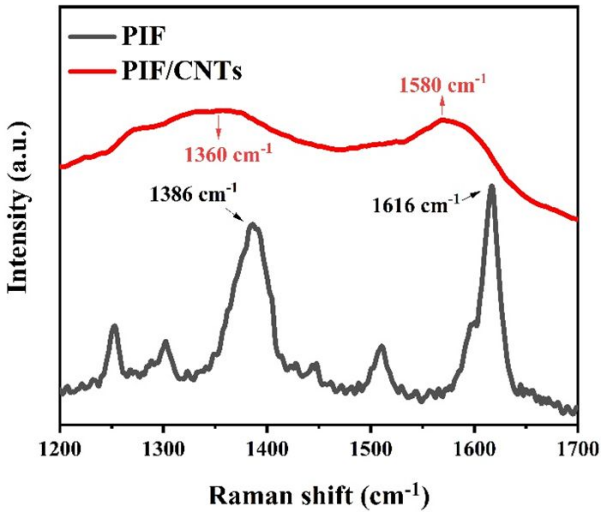

Figure S15. Raman spectra of pure PIF aerogel and PIF/CNTs composite aerogel.

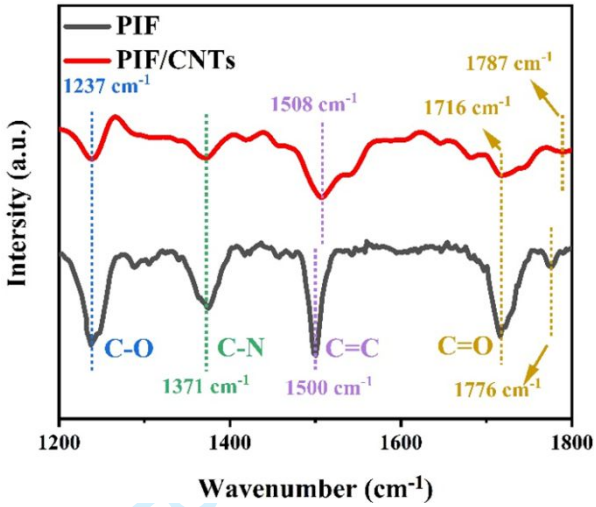

Figure S16. FT-IR spectra of pure PIF aerogel and PIF/CNTs composite aerogel.

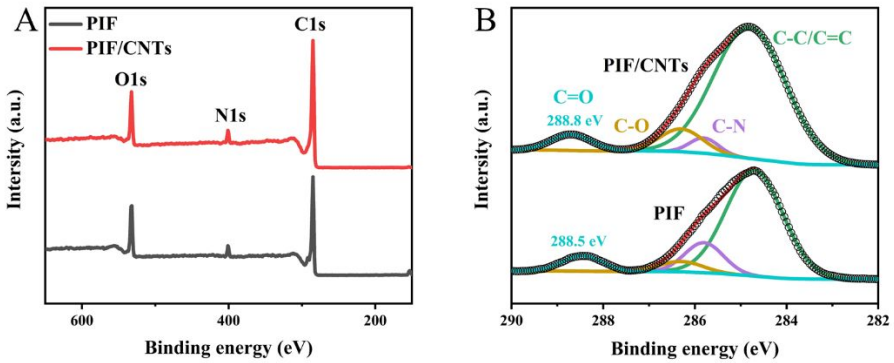

Figure S17. (A) XPS spectra and (B) XPS high-resolution spectra of C1s of pure PIF aerogel and PIF/CNTs composite aerogel.

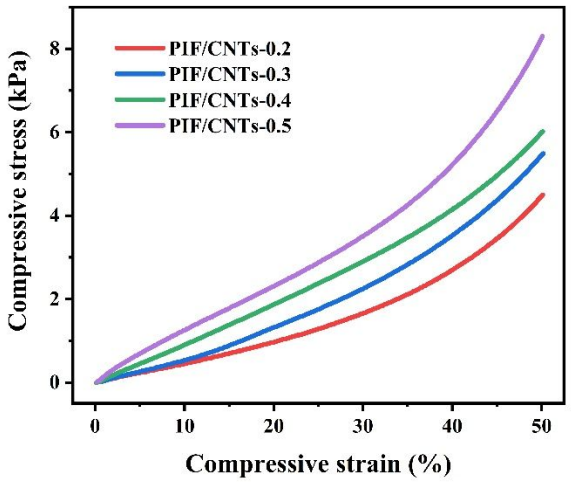

Figure S18. Stress-strain curve of PIF/CNTs composite aerogel with different CNTs loadings upon 50% strain.

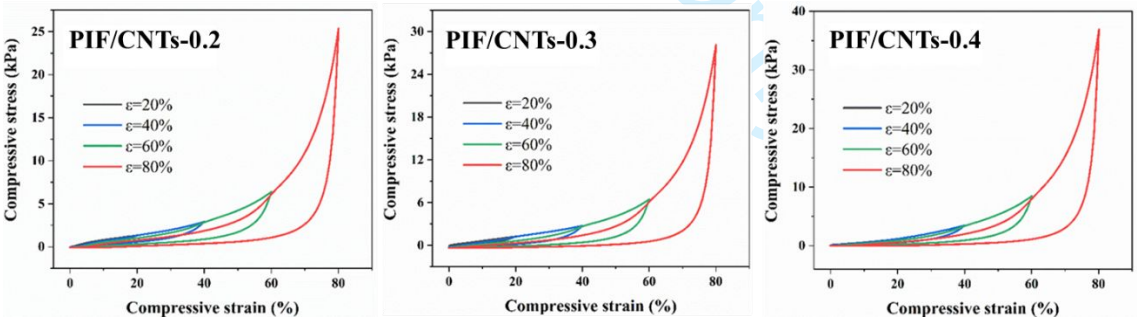

Figure S19. Stepwise stress–strain curve of PIF/CNTs composite aerogel with different CNTs loadings.

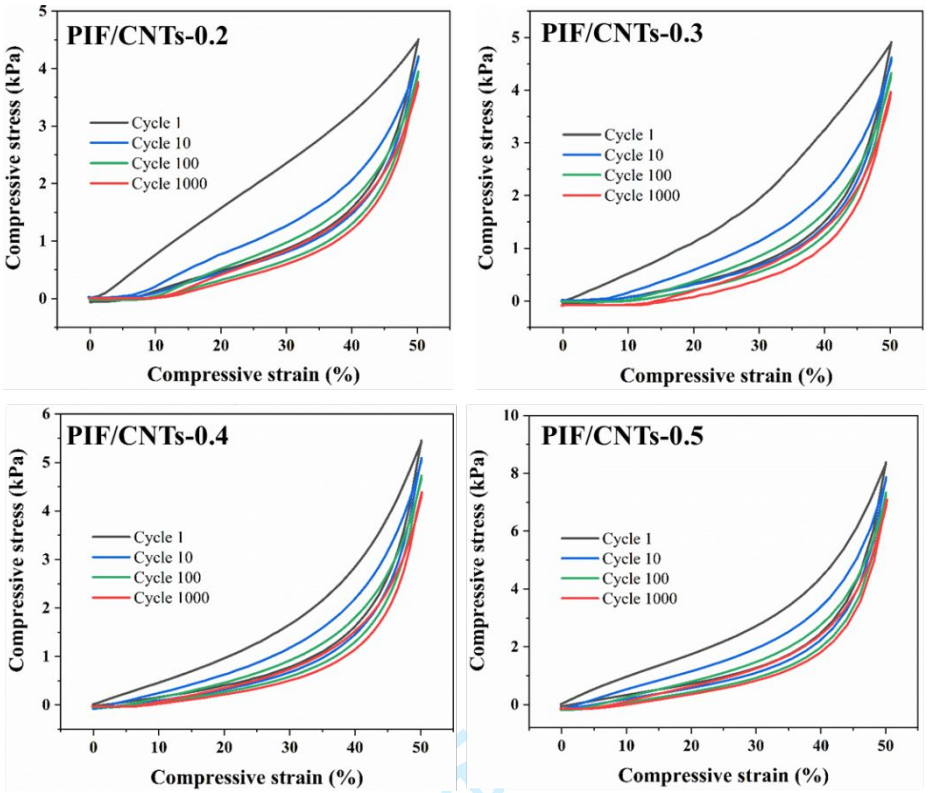

Figure S20. Stress–strain curve of PIF/CNTs composite aerogel with different CNTs content over 1000 cycles.

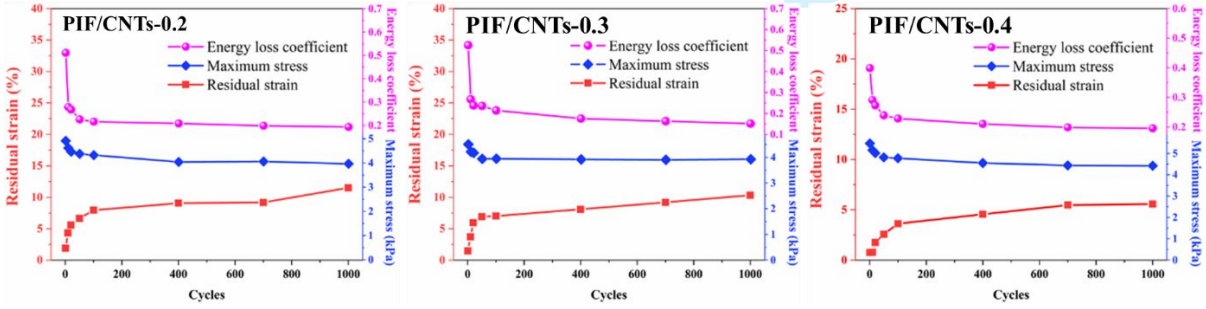

Figure S21. Corresponding residual strain, maximum stress and energy loss coefficient of PIF/CNTs composite aerogel with different CNTs content over 1000 cycles.

Figure S22. Digital photo of the instantaneous compression process of the PIF/CNTs composite aerogel at a speed of 500 mm/min.

Graphical Abstract

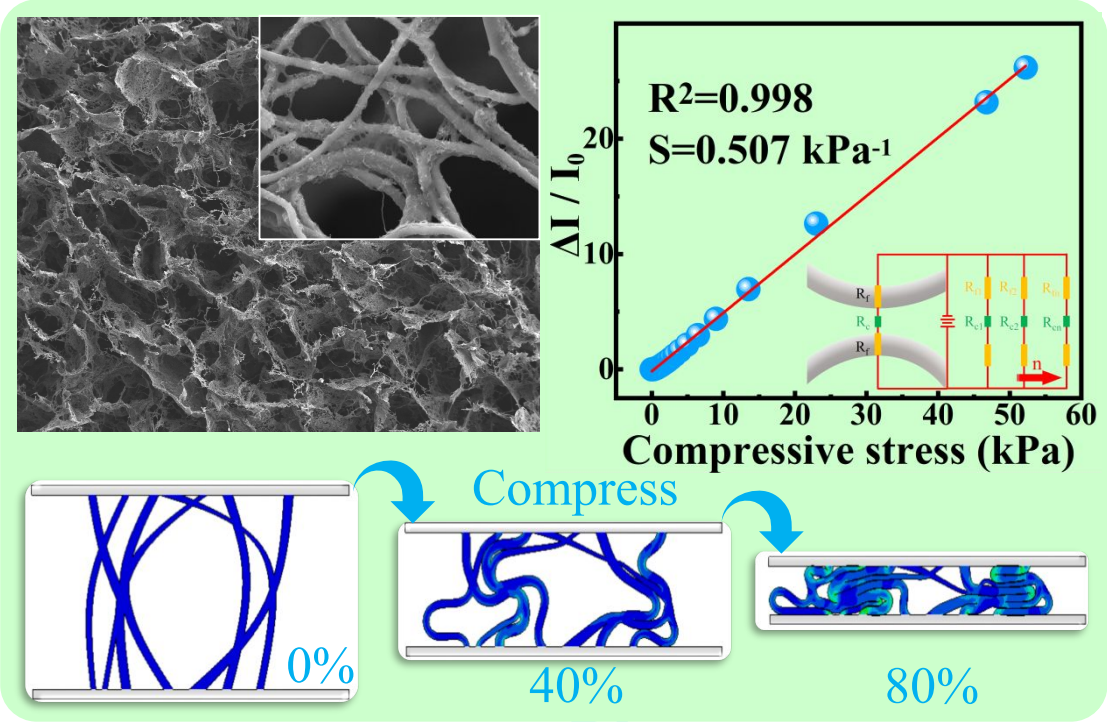

The polyimide fiber (PIF/CNTs) composite aerogel based on the unique spider web-like hierarchical fiber network structure exhibits extremely high compressibility (up to 90% strain), elasticity, and an ultrawide linear sensing range (0.01–53.34 kPa).